nature neuroscience

Retinal origin of orientation maps in visual cortex

Se-Bum Paik[1] & Dario L Ringach[1,2]

The orientation map is a hallmark of primary visual cortex in higher mammals. It is not yet known how orientation maps develop, what function they have in visual processing and why some species lack them. Here we advance the notion that quasi-periodic orientation maps are established by moiré interference of regularly spaced ON- and OFF-center retinal ganglion cell mosaics. A key prediction of the theory is that the centers of iso-orientation domains must be arranged in a hexagonal lattice on the cortical surface. Here we show that such a pattern is observed in individuals of four different species: monkeys, cats, tree shrews and ferrets. The proposed mechanism explains how orientation maps can develop without requiring precise patterns of spontaneous activity or molecular guidance. Further, it offers a possible account for the emergence of orientation tuning in single neurons despite the absence of orderly orientation maps in rodents species.

It has long been known that the primary visual cortex of higher mammals is organized into functional maps[1]. One of the most studied is the orientation map, which captures the preferred orientation of neurons across the cortical surface. Optical imaging methods[2,3] have revealed that preferred orientation on the cortex changes continuously in a quasi-periodic fashion, except at intermittent point discontinuities (pinwheels) and line discontinuities (fractures), where orientation preference seems to jump[4–6]. Although much effort has been devoted to the study of cortical maps, we still lack a full account of how they develop and what part they play in normal visual processing[7–9].

The quasi-periodicity of cortical maps has been postulated to establish sensory modules that serve to process signals from a single location on the visual field by a heterogeneous set of receptive fields[8]. However, it is now recognized that some species lack orientation maps despite having simple cells that show normal receptive field structure and orientation selectivity[10,11]. Similarly, the expression of ocular dominance columns varies widely across individual members of a species[12] and is entirely absent in some species that, nevertheless, show normal evoked potentials to stereoscopic stimuli[13]. Such findings raise doubts about the functional significance of cortical maps in visual processing.

Important clues regarding the wiring of orientation maps and receptive fields of neurons are found in early development. In kittens, orientation-tuned responses can be measured as soon as the kittens open their eyes about a week after birth[14]. Orientation columns (the clustering of cells with similar preferences) and maps are also present at this early stage. This organization can be established without exposure to normal visual experience[14–17], which is otherwise needed for receptive fields and maps to reach full maturation[15,18].

The development of the spatial structure of cortical receptive fields also offers important hints. A key observation is that simple-cell receptive fields seem to develop without an intermediate phase of segregation between ON and OFF subregions[19,20] (as assumed by dominant developmental models[21–23]). This is surprising because the classical view holds that numerous geniculate afferents, with overlapping ON- and OFF-center receptive fields, must be sorted out by cortical neurons to generate simple cells with segregated ON and OFF subregions[24]. However, this segregation process has never been observed experimentally. Instead, the available data in cats indicate that the ratio of simple cells (which have one or more segregated subregions) to complex cells (which have overlapping ON and OFF responses) remains approximately constant during development[19,20]. This suggests that cortical cells have a normal receptive field organization as soon as it is possible to record visually driven responses from them[14,20,25].

How can receptive fields and maps be wired so early in development? Our study builds upon the statistical connectivity hypothesis, which provides some initial answers to this question[26,27]. The basic idea is that receptive fields and orientation maps in the cortex are constrained by the spatial distribution of ON- and OFF-center receptive fields in retinal mosaics[26], a notion that goes back to pioneering work in the 1980s[28,29]. These constraints seed the structure of receptive fields and maps in the cortex upon which other developmental processes, such as activity-dependent refinement and maintenance, act during the critical period.

The present work advances the theory by answering an important question: how does the model generate periodic orientation maps? Here we show that the periodicity of the map can arise from the moiré interference pattern of retina ganglion cell (RGC) mosaics, which is mirrored in the lateral geniculate nucleus (LGN) and generates a quasi-periodic input into the cortex. As we will see, this insight provides a simple explanation for the generation of simple-cell receptive fields and orientation maps, making new predictions about their organization.

A central prediction of the model is that iso-orientation domains should lie on a hexagonal lattice on the cortical surface. Here we show that this arrangement is observed in all four different species examined so far—monkeys, cats, ferrets and tree shrews—providing

[1]Department of Neurobiology, David Geffen School of Medicine, University of California, Los Angeles, California, USA. [2]Department of Psychology, University of California, Los Angeles, California, USA. Correspondence should be addressed to D.L.R. (dario@ucla.edu).

Received 28 January; accepted 23 March; published online 29 May 2011; doi:10.1038/nn.2824

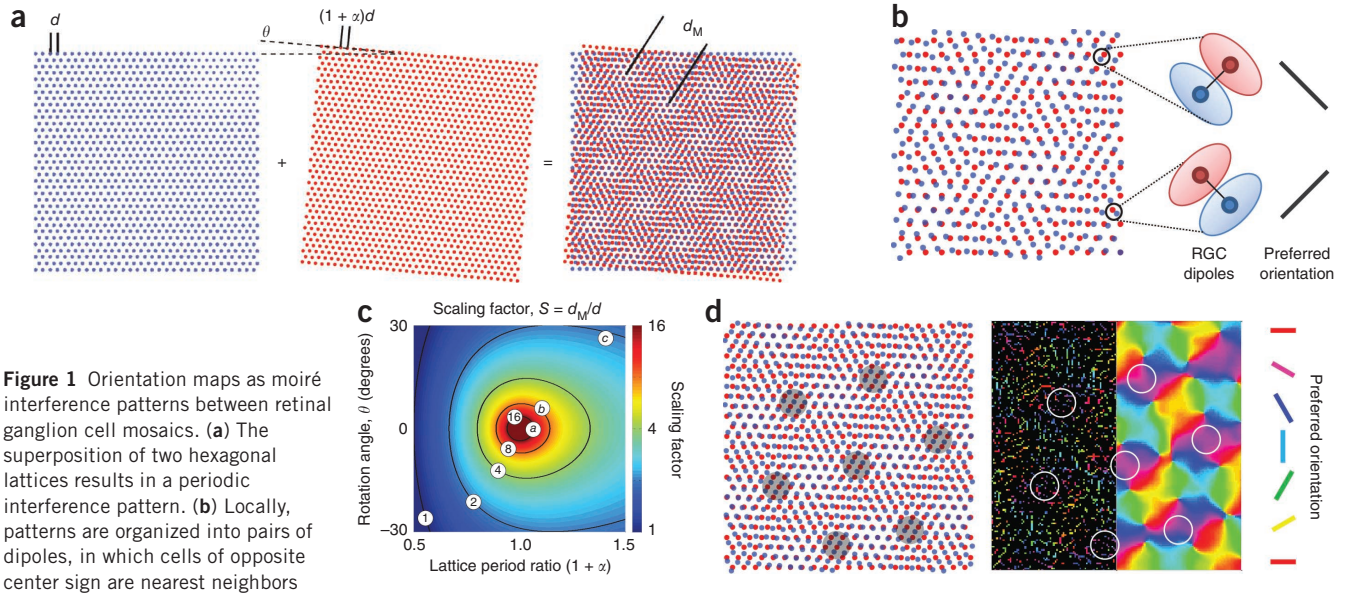

Figure 1 Orientation maps as moiré interference patterns between retinal ganglion cell mosaics. (**a**) The superposition of two hexagonal lattices results in a periodic interference pattern. (**b**) Locally, patterns are organized into pairs of dipoles, in which cells of opposite center sign are nearest neighbors of each other. Cortical pooling of inputs from a dipole (relayed by the LGN) would result in simple-cell receptive fields with side-by-side ON and OFF subregions. (**c**) The period of the interference pattern is a function of the ratio between the lattice spacing in the two mosaics and their relative orientation. The operating points *a*, *b* and *c* lead to scaling factors of 21, 8.1 and 2.2, respectively, and these operating regimes are also used in the following figures. (**d**) Example of an orientation map generated from a moiré interference pattern. The left panel shows the moiré interference pattern between ON- and OFF-center receptive fields. Shaded areas on the moiré interference pattern show that dipoles with the same orientation arrange themselves as vertices of a hexagonal lattice pattern (see also **Fig. 2c**). In the right panel, which represents the same area shown by the pattern on the left, the resulting cortical orientation tuning is shown in two ways. The left half of the map shows the preferred orientation of well tuned cortical cells (orientation selectivity index >0.25; see Online Methods) coded by their preferred orientation. The smooth map in the right half is obtained by Gaussian filtering of these strongly tuned orientation signals (see Online Methods for details). Dipole orientation (left panel) determines the preferred orientation of the best-tuned neurons in the cortex (right panel). Outlined white circles on the right panel correspond to the same iso-orientation domains depicted on the interference pattern on the left.

experimental support for the model. Moreover, our analyses demonstrate that the model admits regimes in which orientation tuning in individual cells can arise without the emergence of an orderly orientation map, potentially extending the theory to incorporate rodent species.

RESULTS

Orientation maps as moiré interference of RGC mosaics

We propose that the cortical orientation map is seeded by moiré interference[30] between ON- and OFF-center receptive fields of one class of ganglion cell in the retina (**Fig. 1**). We introduce our model by considering an ideal case where the locations of ON- and OFF-center receptive fields lie at the vertices of perfect hexagonal lattices. This is a sensible starting point because it is known that their local structure is a noisy hexagonal lattice[28], as inferred from the fact that the angle formed by a cell body with its neighbors of the same sign has modes at multiples of 60 degrees (see **Supplementary Fig. 1** for another demonstration). The ON and OFF lattices are also known to be independent from each other in the sense that knowledge of the location of a cell from one sign does not provide information as to the location of cells of the other[31,32]. When two hexagonal lattices are superimposed in such a way, the result is a periodic interference pattern (**Fig. 1a**). An important property of the resulting pattern is that the nearest neighbor of an ON-center cell is an OFF-center cell (and vice versa) (**Fig. 1b**), a feature that is also observed in the statistics of RGC mosaics reconstructed experimentally[28,33]. We call such a pair of opposite-sign, nearest neighbors a dipole and assign to it an orientation that is perpendicular to the line joining the centers of the constituent receptive fields (**Fig. 1b**).

The statistical wiring model posits that pooling inputs of nearby RGC receptive fields (relayed by cells in the LGN[34]) using an isotropic weighting function is sufficient to generate orientation tuning and simple-cell receptive field structure[26,27]. If the input to a cortical cell is dominated by a single RGC dipole, the resulting receptive field will have a structure similar to that of a simple cell, with side-by-side subregions of opposite sign, and its preferred orientation will match that of the dipole (**Fig. 1b**). The receptive fields generated by the model are not always dominated by single dipoles[26], but those satisfying this condition tend to be the ones that are most sharply tuned for orientation (**Fig. 1d**). Thus, the orientation of RGC dipoles provides a good approximation to the structure of the orientation map seeded by the model. This simplification allows us to derive and understand many important properties of the cortical map predicted by the theory in a simple and intuitive manner.

Periodicity of the orientation map

From the preceding discussion it is clear that the period of the orientation map is determined by the period of the moiré pattern itself, d_M (**Fig. 1a**), which is given by[35]

$$d_M = \left(\frac{1+\alpha}{\sqrt{\alpha^2 + 2(1-\cos\theta)(1+\alpha)}} \right) d \equiv S \times d$$

Here d represents the spacing of the first lattice, $(1 + \alpha)d$ is the spacing of the second lattice and θ their relative orientation. We define the scaling factor as the ratio between the period of the interference pattern and that of the lattice, $S \equiv d_M/d$ (**Fig. 1c**). This ratio is

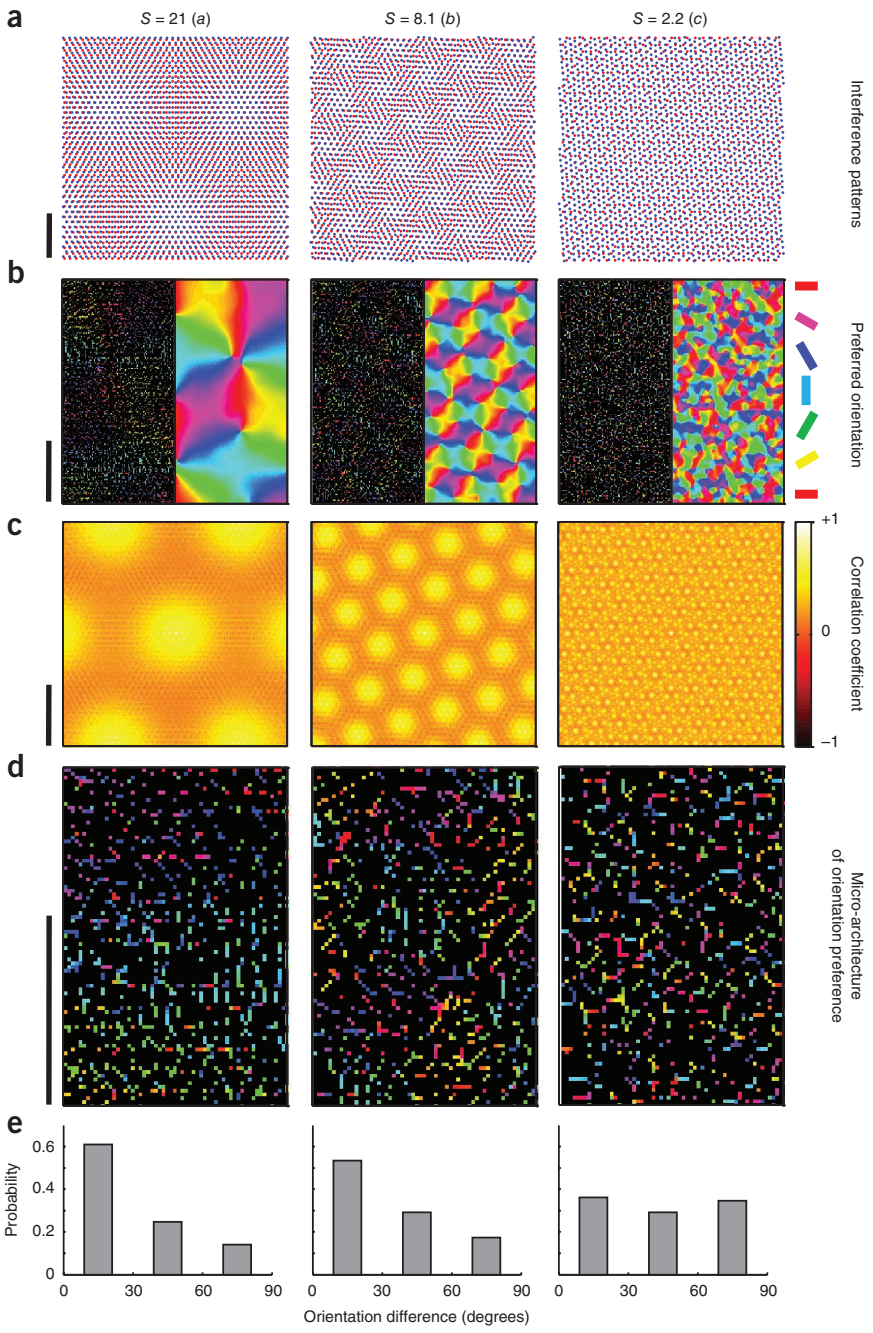

Figure 2 Moiré scaling factor and orientation map periodicity. Each column depicts examples of different scaling factors. The operating regimes illustrated are the ones shown by *a*, *b* and *c* in **Figure 1c**. (**a**) Examples of the resulting moiré interference patterns. (**b**) The preferred orientations of well tuned cells (left) and filtered orientation maps (right). Format as in **Figure 1d**. (**c**) Autocorrelations of orientation maps show hexagonal structure, indicating that iso-orientation domains lie on a hexagonal lattice (see also **Fig. 1d**). (**d**) Enlarged area from the maps in **b** showing the predicted micro-architecture of orientation preference. Preferred orientation changes gradually in the left and middle panels. In the right panel, orientations are distributed as a salt-and-pepper-like pattern. (**e**) Histogram of the orientation differences between pairs of nearby cells (<100 μm) on the cortical surface. Similar orientations cluster in the left and middle panels. In the right panel, preferred orientations at nearby locations are uncorrelated. The uniform distribution of angular differences in the right histogram is a signature of salt-and-pepper organization. Scale bar in **a**, 1 mm on the retinal surface. Scale bars in **b**–**d**, 1 mm of cortical space.

important because it determines how many RGC receptive fields are involved in the construction of one cortical hypercolumn.

The parameters α and θ determine the scaling factor and the operating regime of the model. Operating regimes that yield small values of the scaling factor (less than ~3) generate a salt-and-pepper-like organization, in which neighboring cells have orientations that independent of each other, because the period of the interference pattern becomes comparable to the distance between the centers of the receptive fields of nearest neighbors in the mosaics (**Fig. 2**). Operating regimes with scaling factors between 4 and 16 generate interference patterns that, after the cortical magnification factor is taken into account (see the calculation in **Supplementary Discussion**), can match the periodicity of experimentally measured maps in primates (**Fig. 2**). Regimes near the origin $(\alpha,\theta) = (0,0)$ generate large scaling factors, and, as a consequence, preferred orientation changes very slowly across cortical space (**Fig. 2**).

Orientation maps have hexagonal symmetry

One surprising prediction can be derived from the ideal model by examining the structure of the moiré interference patterns. Each pattern is periodic: all possible orientations appear within one cycle and change smoothly across cortical space (**Fig. 1a**,**d**). The hexagonal symmetry of the interference pattern predicts that (assuming an isotropic magnification factor) locations with the same orientation preference should be arranged in a hexagonal lattice pattern on the cortical surface as well (**Figs. 1d** and **2c**).

We tested this prediction using published orientation maps from different species. In each case, we begin by representing each map as a two-dimensional image $\theta(x,y)$ and compute a two-dimensional (circular) autocorrelation as follows:

$$r(\Delta x,\Delta y) = \frac{1}{N}\sum_{x,y}\left(\left|\exp\left(2i\theta(x,y)\right) + \exp\left(2i\theta\left(x+\Delta x, y+\Delta y\right)\right)\right| - 1\right)$$

In other words, two copies of the same map are shifted relative to each other by $(\Delta x,\Delta y)$ and the agreement between the orientations in the shifted maps is assessed in the region of overlap by an averaged vector resultant (the region of overlap having N pixels). If all the values between two maps in overlapped areas match closely, we obtain a value $r \approx 1$. If the orientations at each location between two maps are orthogonal, $r = -1$.

The autocorrelation functions, evaluated in two individuals of four different species, showed a pattern of discrete, secondary peaks around the origin that resemble a hexagon (**Fig. 3a**) (see also

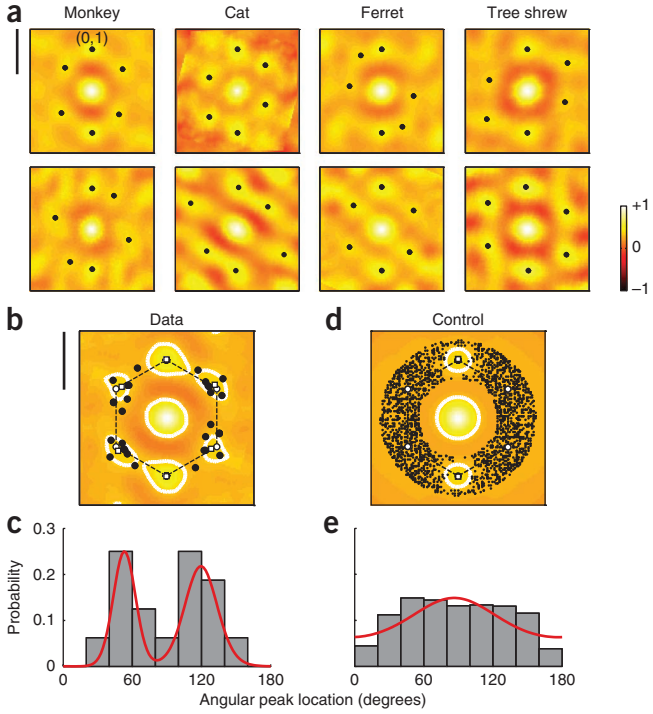

Figure 3 Hexagonal structure of orientation maps. (**a**) The autocorrelation structure of orientation maps are shown for two different animals in four species. Secondary peaks (solid black circles) in the autocorrelation function form an approximate hexagonal structure in all cases. The magnitudes of all of these local maxima are statistically significant (bootstrap analysis, $P < 0.002$). The scale bar equals the orientation map period. (**b**) The average autocorrelation function across all animals shows local peaks (open white squares) that match closely the ones predicted by a perfect hexagonal lattice (open white circles). The solid black circles represent the locations of all the local maxima (shown in panel **a**) after the normalization step. White contour lines are plotted at a correlation coefficient of 0.33 to illustrate the separation of local peaks. The scale bar equals the orientation map period. (**c**) Angular location of local peaks in the autocorrelation function in panel **b** relative to the reference peak. The distribution is bimodal with modes near 60 and 120 degrees, as predicted by the model. Bimodality was established by a mixture of von Mises distributions using the Bayes information criterion to select the order of the model. The red solid line shows the probability distribution of the best fit. (**d**) The same analysis performed on control maps. Here the distribution of local peaks is much more isotropic. (**e**) One component (red line) is sufficient to account for the control data. In **a**–**d** local peaks were considered only if their distances to the origin were within ±33% of the map period.

Supplementary Fig. 2). In each case, the autocorrelation functions are scaled and rotated to map the local peak with the largest magnitude onto the point (0,1) in the plane. The statistical significance of the local peaks is assessed by generating control maps with an isotropic amplitude spectrum matching that of experimental maps and computing the distribution of amplitudes of secondary peaks from such a family of control maps (calculation detailed in **Supplementary Fig. 3**). All the secondary peaks shown in **Figure 3a** as black dots attain a significance level of $P < 0.002$. In other words, the local peaks are very unlikely to have been generated by chance, assuming the null hypothesis that orientation maps are isotropic.

Next, we computed the average autocorrelation function across individuals and species (**Fig. 3b**). The result shows local peaks that very closely match the hexagonal prediction. The distribution of local maxima in the individual cases, superimposed on top of the mean autocorrelation function, cluster around the vertices of the hexagon. This observation can be validated by the distribution of the angular location of the peaks relative to the reference point at (0,1), which is clearly bimodal (**Fig. 3c**). When we fit the angular distribution with a mixture of von Mises components, we find the data are best explained by a mixture of two components (**Fig. 3c**; model selection by Bayesian information criterion). The modes of the components match very well their predicted locations at 60 and 120 degrees. Thus, the angular distribution of local maxima is consistent with that of a hexagonal lattice. When the same analysis is repeated on the control maps, the magnitudes of the local peaks are substantially smaller (as already reflected in the fact that only 1 in 500 control maps attained peaks of similar magnitude by chance). Furthermore, the angular distribution of local peaks whose magnitudes reach statistical significance by chance

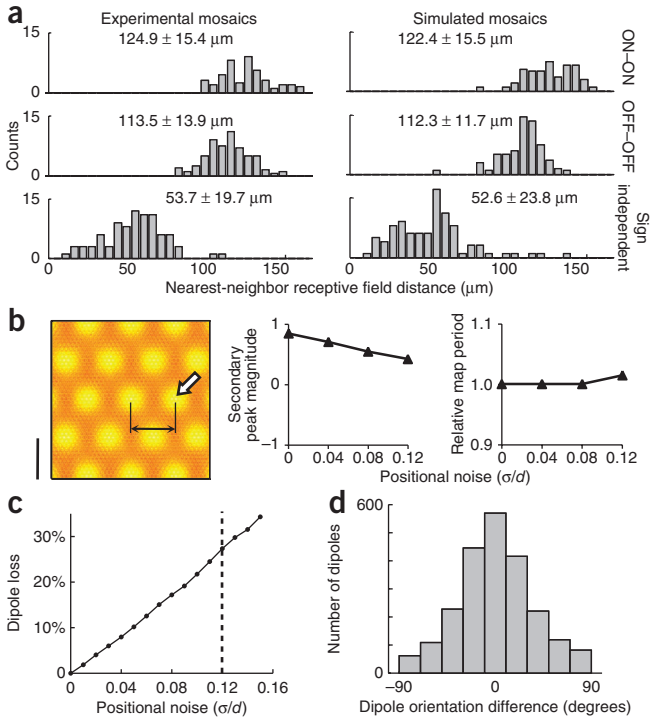

Figure 4 Robustness of seeded map to positional noise. (**a**) The addition of independent Gaussian noise of an appropriate magnitude to the positions of vertices in the hexagonal lattice enables the model RGC mosaic to match the statistics of nearest-neighbor distance distributions observed experimentally, both within and across cell types. The experimental data show the distance between receptive field center locations. The standard deviation of the Gaussian noise required to match these distributions is $\sigma = 0.12d$. (**b**) The periodicity and strength of the seeded structure can be measured by the distance from the origin (black arrows) and magnitude of secondary peaks (white arrow) in the autocorrelation of the orientation map. As noise increases to realistic values, the secondary peak in autocorrelation remains strong and the map period is invariant, showing the robustness of the moiré interference pattern. The map period is plotted normalized to that attained in the absence of positional noise. (**c**) The percentage of ON–OFF dipoles originally present in the noise-free interference pattern that are lost with increasing noise. The vertical line indicates the level required to match nearest-neighbor distributions, $\sigma = 0.12d$. For this value of noise, 27% of the dipoles are lost on average. (**d**) Dipoles that survive the perturbation of their location will have their original orientation perturbed. The histogram shows the distribution of changes in orientation in a dipole from its original orientation at experimental noise values, $\sigma = 0.12d$.

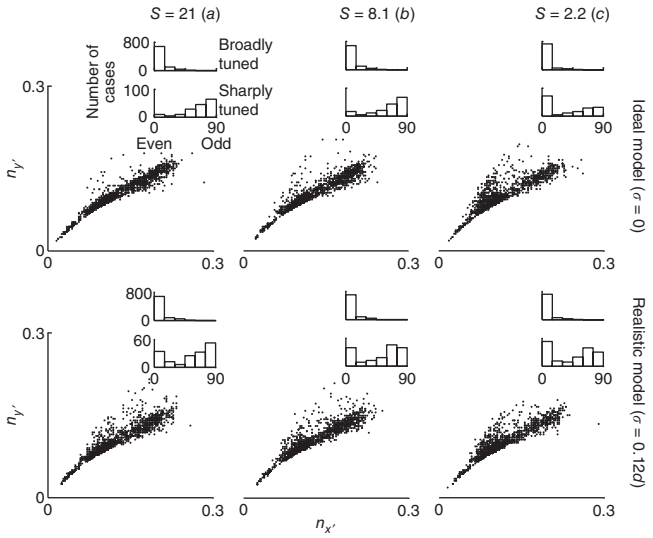

Figure 5 Robustness of receptive field shapes at different operating regimes of the model. Receptive field structure was evaluated by the distribution of $(n_{x'}, n_{y'})$ and of spatial phases of the simulated receptive fields. The distributions are similar for the different operating regimes, even though some do not support the existence of smooth orientation maps. Insets show the distributions of spatial phases in broadly tuned (bottom 50%) and sharply tuned (top 10%) simulated receptive fields.

is almost uniform, with a depletion of points near the reference point that results from the alignment procedure (**Fig. 3d**,**e**). Finally, for comparison, we performed the same analysis on orientation maps generated by an activity-dependent model[36]. We found that this model does not generate autocorrelations with any secondary peaks of statistically significant magnitude ($P > 0.05$; data not shown).

Effects of RGC lattice noise on map periodicity

Of course, RGC mosaics are not perfect hexagonal lattices. This raises the question of whether the proposed mechanism is capable of seeding an orientation map after the addition of realistic amounts of noise in the positions of the RGC receptive fields. We tested this by perturbing the vertices of the hexagonal lattices with independent two-dimensional Gaussian noise to match the nearest-neighbor statistics in experimentally measured mosaics[26]. A ratio between the standard deviation and the average of the lattice spacing of $\sigma/d \approx 0.12$ provides a very good match to the distributions of nearest-neighbor receptive fields in the experimental data (**Fig. 4a**). We find that even with this realistic degree of noise, the interference pattern remains strong enough to generate a periodic orientation map (**Fig. 4b**,**c**). The periodicity of the map can be evaluated by measuring the amplitude and location of the secondary peaks in the autocorrelation of the simulated orientation map as a function of noise (**Fig. 4b**). The normalized period of the map (relative to the ideal case) remains stable (**Fig. 4b**, right) and the magnitude of the secondary peak is positive and substantially larger than zero (**Fig. 4b**, middle), indicating a robust periodic structure.

Insight into the robustness of the seeded map is gained by calculating the number of original dipoles in the interference pattern that are lost as positional noise increases (**Fig. 4c**) and, of those that remain, how much their orientation is perturbed relative to that of their original configuration (**Fig. 4d**). A dipole is defined by two cells of opposite sign that are nearest neighbors of each other. As the positional noise increases the conditions defining a given dipole may cease to hold, in which case we say the dipole is 'lost'. Simulations show a roughly linear increase in the fraction of dipoles lost with increasing noise, reaching a value of 27% for realistic values (**Fig 4c**). Thus, about 73% of the dipoles of the original pattern survive. Of those dipoles remaining, their orientation is close to that of their original configuration (**Fig. 4d**). These analyses clarify the reasons behind the robustness of the seeded map to positional noise. An example of an interference pattern with realistic noise and the resulting orientation map is provided in **Supplementary Figure 4**.

Robustness of receptive field structure to positional noise

What is the spatial structure of simple-cell receptive fields generated by the model, and how are they affected by the presence of positional noise? To answer this question, we fitted a two-dimensional Gabor function to the simulated simple-cell receptive fields at randomly chosen cortical sites. The Gabor function was defined by[37]:

$$h(x', y') = A \exp\left(-\left(x'/\sqrt{2}\sigma_{x'}\right)^2 - \left(y'/\sqrt{2}\sigma_{y'}\right)^2\right)\cos\left(2\pi f x' + \phi\right)$$

where the coordinate system (x', y') is obtained by translating the original by (x_0, y_0) and rotating it by γ.

$$x' = (x - x_0)\cos\gamma + (y - y_0)\sin\gamma$$
$$y' = -(x - x_0)\sin\gamma + (y - y_0)\cos\gamma$$

In the (x', y') plane, the modulation of the sinusoidal function is along the x' axis, and $\sigma_{x'}$ and $\sigma_{y'}$ represent the width of the Gaussian envelope along each axis respectively, f represents spatial frequency and ϕ is the spatial phase. Even-symmetric profiles are obtained for $\phi = 0$ and odd-symmetric profiles are obtained for $\phi = \pi/2$.

We analyzed the data by looking at the distribution of $n_{x'} = \sigma_{x'} f$ and $n_{y'} = \sigma_{y'} f$, as previously done in the experimental study of primate data[37]. These numbers can be thought as a measure of the width of the Gaussian envelope along each axis in units of the period of the underlying sinusoidal grating.

We found that the distribution of $n_{x'}$ and $n_{y'}$ remains largely unaffected by changes in scaling factor and amount of RGC lattice noise (**Fig. 5**). The reason for this is that the local structure of receptive fields is solely dependent on the statistics of nearest-neighbor distributions (**Fig. 4a**). So long as there is a high probability that the nearest neighbor of one receptive field is another of the opposite sign, the model will generate dipoles that can induce similar families of simple-cell receptive fields. The theory thus admits a regime in which single neurons can be well tuned for orientation despite the absence of a smooth orientation map, as is observed in rodents (**Fig. 2**, right column).

The distribution of spatial phases of the predicted receptive fields is also of interest (**Fig. 5**). The simulations indicate that odd-symmetric receptive fields tend to be well tuned for orientation. This is due to the fact that inputs to a cell dominated by a single dipole will generate a well tuned, odd-symmetric receptive field. Even-symmetric receptive fields can be either broadly tuned (with one effective subregion) or sharply tuned (with three effective subregions of alternating signs). The tendency for well tuned cells in the model to shift their spatial phase toward odd symmetry is consistent with experimental observation[37].

DISCUSSION

Where do orientation maps come from? Here we put forward the notion that periodic orientation maps arise from the moiré interference pattern of quasi-regular retinal mosaics (**Fig. 1**). A central prediction

of the model is that iso-orientation domains should be arranged approximately in a hexagonal lattice on the cortical surface. Indeed, we found this property in all four different species tested: ferrets, tree shrews, cats and monkeys. Such a universal property of maps provides support for a single mechanism at work in different species and one that is consistent with the model's prediction. A recently published geometric analysis of orientation columns provides further evidence of their hexagonal structure[38].

Several puzzling findings of visual development are parsimoniously explained by the model. Moiré interference explains how cortical receptive fields and maps may arise even in the absence of precisely structured activity in the developing thalamus[22,36,39]. This is because RGC mosaics themselves can develop without the need for visual experience[40]. The theory solves the dilemma of how simple cells can arise in early development without an intermediate phase of segregation between ON- and OFF-center inputs[19,20]. It further accounts for a segregation of ON- and OFF-center afferents into cortical domains[41]. Both results are a consequence of the limited overlap between nearest neighbors in retinal mosaics.

The emergence of orientation columns is also explained by the model, as in this scheme cortical neurons in a column receive inputs from the same set of RGCs and thus their receptive fields are constrained in the same way. If the input partly determines the preferred orientation of the cortical column, the emergence of orientation columns is easily understood. Experimental support for this idea is provided by the recent finding that the distribution of ON- and OFF-center receptive fields in the LGN predicts the orientation preference of its target cortical column[42]. This result is noteworthy because, it if holds across all cortical positions, it implies that the orientation map is already coded in the LGN. Competing theories based on activity-dependent wiring do not account for the orientation bias present in the LGN input and how it can successfully predict the preferred orientation of their cortical targets.

During development, a diverse set of receptive fields is observed in the thalamus, some of which show ON and OFF subregions and orientation tuning[43]. Such an intermediate stage is consistent with our model in that, before the pruning of retino-geniculate inputs, thalamic cells may pool from receptive fields of both signs, resulting in receptive fields similar to those generated by the model. Reference 43 postulated that this intermediate stage, along with activity-dependent learning, could generate orientation-tuned cells in the cortex. We note that unless one also incorporates the key constraints established by the retinal input, such a mechanism alone fails to account for the emergence of orientation columns.

The simultaneous mapping of simple-cell receptive fields in a population of nearby cortical cells can also serve to test our hypothesis that receptive fields are constructed from a limited number of inputs. For example, a recent two-photon imaging of mouse visual cortex reveals that nearby simple-cell receptive fields often share common subregions with the same location and shape[44], consistent with the notion that they are all constructed from a limited input[26].

The model admits a regime in which single cells are well tuned despite the absence of an orientation map. This was demonstrated by the invariance of the receptive field structure (documented by the distribution of $(n_{x'}, n_{y'})$ values) with changes in the scaling factor and positional noise (**Fig. 5**). The theory thus offers a potential explanation for how the properties of simple-cell receptive fields could be similar in mice, cats and monkeys[37,45]. We must exercise caution as a small scaling factor is only one possible explanation of this phenomenon. In general, if the emergence of the moiré interference pattern is disrupted for any reason, it will lead to a failure in the creation of orientation maps. To some extent this situation may already arise at the fovea, where dedicated one-to-one lines for ON- and OFF-center receptive fields increase their overlap compared to those in parafovea. Indeed, near the fovea the orientation map appears disrupted in double-label 2-deoxyglucose studies[46], which is also consistent with the fact that orientation-tuned neurons near the fovea are fewer and more broadly tuned than those in the parafovea[47].

The present scope of the model is limited to explaining how the inputs from the contralateral eye, which invade the cortex ahead of those from the ipsilateral eye, could establish an initial blueprint for receptive fields and maps. The orientation map is expected to change as input from the ipsilateral eye is accommodated and both orientation maps come into register, but not so much as to erase all vestiges of the initial map organization[15]. Even during this process, the geniculate inputs will continue to constrain the range of preferred orientations attainable at any cortical site from any given eye. In other words, these constraints ought to be taken into account in models that study activity-dependent matching of the orientation maps of the two eyes.

Finally, the theory predicts the existence of what could be called orientation scotomas: at some locations, the cortex cannot represent every orientation equally well. This results from the fact that limited retinal resources at some locations prohibit the implementation of receptive fields with a complete set of preferred orientations (**Fig. 1d**). We are now testing this prediction by mapping human orientation discrimination thresholds of very small stimuli in the far periphery. A confirmation of orientation scotomas would provide further support for the theory and challenge the present view of the cortex as analyzing the local image by a homogeneous set of filters tuned to different orientations. Although the preceding hypothesis is controversial, we note that a previous study[48] found that pairs of cells in the cortex must have their receptive field centers one receptive field diameter apart to ensure their orientation preferences are, on average, orthogonal to one another, a finding consistent with the notion of orientation scotomas.

To summarize, moiré interference offers a mechanism for the initial seeding of a periodic orientation map and simple-cell receptive fields that does not require specific patterns of spontaneous thalamic activity, the presence of molecular markers or cortical scaffolding. The simplicity of the model, the parsimonious explanations it offers to several key findings, and the recent confirmation of several of its predictions are all encouraging. The hexagonal structure in the autocorrelations of orientation maps of various species now provides additional support for our hypothesis, which awaits its ultimate test—an experiment that can reveal a correlation between the structure of the RGC mosaics and the orientation maps measured in the same individuals.

METHODS

Methods and any associated references are available in the online version of the paper at http://www.nature.com/natureneuroscience/.

Note: Supplementary information is available on the Nature Neuroscience website.

ACKNOWLEDGMENTS

We are grateful to A. Benucci and M. Carandini (University College London) for sharing their imaging data of cat primary visual cortex, supported by research grant EY017396 to M. Carandini. We also thank D. Fitzpatrick (Max Planck Florida Institute), L. White (Duke University), W. Bosking (University Texas at Austin) and Y. Li (UC Berkeley) for sharing existing ferret and tree shrew maps. We thank M. Carandini, D. Fitzpatrick, R. Shapley, J.-M. Alonso and E. Callaway for providing comments on earlier versions of this manuscript. This work was supported by research grant EY018322 (D.L.R.).

AUTHOR CONTRIBUTIONS
Both S.-B.P. and D.L.R. were responsible for the theoretical concepts, computer simulations and writing.

COMPETING FINANCIAL INTERESTS
The authors declare no competing financial interests.

Published online at http://www.nature.com/natureneuroscience/.
Reprints and permissions information is available online at http://www.nature.com/reprints/index.html.

1. Hubel, D.H. & Wiesel, T.N. Ferrier lecture. Functional architecture of macaque monkey visual cortex. *Proc. R. Soc. Lond. B* **198**, 1–59 (1977).
2. Blasdel, G.G. & Salama, G. Voltage-sensitive dyes reveal a modular organization in monkey striate cortex. *Nature* **321**, 579–585 (1986).
3. Ts'o, D.Y., Frostig, R.D., Lieke, E.E. & Grinvald, A. Functional organization of primate visual cortex revealed by high resolution optical imaging. *Science* **249**, 417–420 (1990).
4. Obermayer, K. & Blasdel, G.G. Geometry of orientation and ocular dominance columns in monkey striate cortex. *J. Neurosci.* **13**, 4114–4129 (1993).
5. Bonhoeffer, T. & Grinvald, A. The layout of iso-orientation domains in area-18 of cat visual-cortex—optical imaging reveals a pinwheel-like organization. *J. Neurosci.* **13**, 4157–4180 (1993).
6. Bonhoeffer, T. & Grinvald, A. Iso-orientation domains in cat visual-cortex are arranged in pinwheel-like patterns. *Nature* **353**, 429–431 (1991).
7. Purves, D., Riddle, D.R. & Lamantia, A.S. Iterated patterns of brain circuitry (or how the cortex gets its spots). *Trends Neurosci.* **15**, 362–368 (1992).
8. Horton, J.C. & Adams, D.L. The cortical column: a structure without a function. *Phil. Trans. R. Soc. B* **360**, 837–862 (2005).
9. Van Hooser, S.D. Similarity and diversity in visual cortex: is there a unifying theory of cortical computation? *Neuroscientist* **13**, 639–656 (2007).
10. Ohki, K., Chung, S., Ch'ng, Y.H., Kara, P. & Reid, R.C. Functional imaging with cellular resolution reveals precise micro-architecture in visual cortex. *Nature* **433**, 597–603 (2005).
11. Van Hooser, S.D., Heimel, J.A.F., Chung, S., Nelson, S.B. & Toth, L.J. Orientation selectivity without orientation maps in visual cortex of a highly visual mammal. *J. Neurosci.* **25**, 19–28 (2005).
12. Adams, D.L. & Horton, J.C. Capricious expression of cortical columns in the primate brain. *Nat. Neurosci.* **6**, 113–114 (2003).
13. Livingstone, M.S., Nori, S., Freeman, D.C. & Hubel, D.H. Stereopsis and binocularity in the squirrel-monkey. *Vision Res.* **35**, 345–354 (1995).
14. Hubel, D.H. & Wiesel, T.N. Receptive fields of cells in striate cortex of very young, visually inexperienced kittens. *J. Neurophysiol.* **26**, 994–1002 (1963).
15. Crair, M.C., Gillespie, D.C. & Stryker, M.P. The role of visual experience in the development of columns in cat visual cortex. *Science* **279**, 566–570 (1998).
16. Chapman, B., Stryker, M.P. & Bonhoeffer, T. Development of orientation preference maps in ferret primary visual cortex. *J. Neurosci.* **16**, 6443–6453 (1996).
17. Gödecke, I., Kim, D.S., Bonhoeffer, T. & Singer, W. Development of orientation preference maps in area 18 of kitten visual cortex. *Eur. J. Neurosci.* **9**, 1754–1762 (1997).
18. White, L.E., Coppola, D.M. & Fitzpatrick, D. The contribution of sensory experience to the maturation of orientation selectivity in ferret visual cortex. *Nature* **411**, 1049–1052 (2001).
19. Albus, K. & Wolf, W. Early post-natal development of neuronal function in the kitten's visual-cortex: a laminar analysis. *J. Physiol.* **348**, 153–185 (1984).
20. Braastad, B.O. & Heggelund, P. Development of spatial receptive-field organization and orientation selectivity in kitten striate cortex. *J. Neurophysiol.* **53**, 1158–1178 (1985).
21. Miller, K.D. Development of orientation columns via competition between on-center and off-center inputs. *Neuroreport* **3**, 73–76 (1992).
22. Ohshiro, T. & Weliky, M. Simple fall-off pattern of correlated neural activity in the developing lateral geniculate nucleus. *Nat. Neurosci.* **9**, 1541–1548 (2006).
23. Swindale, N.V. The development of topography in the visual cortex: a review of models. *Network* **7**, 161–247 (1996).
24. Reid, R.C. & Alonso, J.M. Specificity of monosynaptic connections from thalamus to visual-cortex. *Nature* **378**, 281–284 (1995).
25. Sherk, H. & Stryker, M.P. Quantitative study of cortical orientation selectivity in visually inexperienced kitten. *J. Neurophysiol.* **39**, 63–70 (1976).
26. Ringach, D.L. Haphazard wiring of simple receptive fields and orientation columns in visual cortex. *J. Neurophysiol.* **92**, 468–476 (2004).
27. Ringach, D.L. On the origin of the functional architecture of the cortex. *PLoS ONE* **2**, e251 (2007).
28. Wässle, H., Boycott, B.B. & Illing, R-B. Morphology and mosaic of on-beta and off-beta cells in the cat retina and some functional considerations. *Proc. R. Soc. Lond. B* **212**, 177–195 (1981).
29. Soodak, R.E. The retinal ganglion-cell mosaic defines orientation columns in striate cortex. *Proc. Natl. Acad. Sci. USA* **84**, 3936–3940 (1987).
30. Amidror, I. *The Theory of the Moiré Phenomenon* (Kluwer Academic, Norwell, Massachusetts, USA, 2000).
31. Rockhill, R.L., Euler, T. & Masland, R.H. Spatial order within but not between types of retinal neurons. *Proc. Natl. Acad. Sci. USA* **97**, 2303–2307 (2000).
32. Eglen, S.J., Diggle, P.J. & Troy, J.B. Homotypic constraints dominate positioning of on- and off-center beta retinal ganglion cells. *Vis. Neurosci.* **22**, 859–871 (2005).
33. Gauthier, J.L. *et al.* Uniform signal redundancy of parasol and midget ganglion cells in primate retina. *J. Neurosci.* **29**, 4675–4680 (2009).
34. Usrey, W.M., Reppas, J.B. & Reid, R.C. Specificity and strength of retinogeniculate connections. *J. Neurophysiol.* **82**, 3527–3540 (1999).
35. Blair, H.T., Welday, A.C. & Zhang, K. Scale-invariant memory representations emerge from moiré interference between grid fields that produce theta oscillations: a computational model. *J. Neurosci.* **27**, 3211–3229 (2007).
36. Miller, K.D. A model for the development of simple cell receptive-fields and the ordered arrangement of orientation columns through activity-dependent competition between ON- and OFF-center inputs. *J. Neurosci.* **14**, 409–441 (1994).
37. Ringach, D.L. Spatial structure and symmetry of simple-cell receptive fields in macaque primary visual cortex. *J. Neurophysiol.* **88**, 455–463 (2002).
38. Muir, D.R. *et al.* Embedding of cortical representations by the superficial patch system. *Cerebral Cortex*, 10.1093/cercor/bhq290 (7 March 2011).
39. Miller, K.D., Erwin, E. & Kayser, A. Is the development of orientation selectivity instructed by activity? *J. Neurobiol.* **41**, 44–57 (1999).
40. Anishchenko, A. *et al.* Receptive field mosaics of retinal ganglion cells are established without visual experience. *J. Neurophysiol.* **103**, 1856–1864 (2010).
41. Jin, J.Z. *et al.* On and off domains of geniculate afferents in cat primary visual cortex. *Nat. Neurosci.* **11**, 88–94 (2008).
42. Jin, J., Wang, Y., Swadlow, H.A. & Alonso, J.M. Population receptive fields of ON and OFF thalamic inputs to an orientation column in visual cortex. *Nat. Neurosci.* **14**, 232–238 (2011).
43. Tavazoie, S.F. & Reid, R.C. Diverse receptive fields in the lateral geniculate nucleus during thalamocortical development. *Nat. Neurosci.* **3**, 608–616 (2000).
44. Smith, S.L. & Hausser, M. Parallel processing of visual space by neighboring neurons in mouse visual cortex. *Nat. Neurosci.* **13**, 1144–1149 (2010).
45. Niell, C.M. & Stryker, M.P. Highly selective receptive fields in mouse visual cortex. *J. Neurosci.* **28**, 7520–7536 (2008).
46. Vanduffel, W., Tootell, R.B.H., Schoups, A.A. & Orban, G.A. The organization of orientation selectivity throughout macaque visual cortex. *Cereb. Cortex* **12**, 647–662 (2002).
47. Poggio, G.F., Baker, F.H., Mansfield, R.J., Sillito, A. & Grigg, P. Spatial and chromatic properties of neurons subserving foveal and parafoveal vision in rhesus monkey. *Brain Res.* **100**, 25–59 (1975).
48. Das, A. & Gilbert, C.D. Distortions of visuotopic map match orientation singularities in primary visual cortex. *Nature* **387**, 594–598 (1997).

ONLINE METHODS

The simulations were performed using the statistical wiring model published earlier. We briefly summarize the algorithm here and refer the reader for justification of the parameters selected to our earlier work[26,27].

Structure of retinal ganglion cell mosaics. Simulated RGC mosaics were generated by adding various amount of random displacement to each vertex of a hexagonal lattice that represents the position of ON- and OFF-center receptive fields[26]. The centers of RGC receptive field position vectors are defined by

$$\mathbf{r}_{ij}^{OFF} = d\,\mathbf{L}_{ij} + \boldsymbol{\eta}_{ij}$$
$$\mathbf{r}_{ij}^{ON} = (1+\alpha)\,d\,R_\theta \mathbf{L}_{ij} + \boldsymbol{\eta}_{ij} + \boldsymbol{\eta}_0$$

Here d represents the grid spacing for the OFF mosaic, $(1 + \alpha)d$ represents the grid spacing for the ON mosaic, the matrix

$$R_\theta = \begin{bmatrix} \cos\theta & \sin\theta \\ -\sin\theta & \cos\theta \end{bmatrix}$$

represents the relative rotation between the ON and OFF mosaics, $\boldsymbol{\eta}_{ij}$ represents two-dimensional, Gaussian (independent and identically distributed) noise with a standard deviation σ, and $\mathbf{L}_{ij}$ are the vertices of a hexagonal grid

$$\mathbf{L}_{ij} = \frac{1}{2}\begin{bmatrix} 1 & 1 \\ \sqrt{3} & -\sqrt{3} \end{bmatrix}\begin{bmatrix} i \\ j \end{bmatrix} \quad i, j = 0, \pm 1, \pm 2, \cdots$$

The standard deviation of the noise, σ, is conveniently expressed as a fraction of the grid spacing, d. The noise-free ideal model corresponds to $\sigma = 0$. A random relative spatial shift between the two mosaics $\boldsymbol{\eta}_0$ can be added. However, except for the particular case where $\alpha = 0$, this has no consequence for the results because a rotation and translation can be written as a rotation around a different center.

To calculate nearest-neighbor statistics in experimental mosaics, we used digitized maps of receptive field reconstructions from the macaque monkey retina, published in ref. 33, modeling the center of the receptive fields as a two-dimensional Gaussian with a standard deviation of 60 μm in retinal space.

Statistical connectivity and receptive field computation. The statistical wiring model includes a stochastic component that allows cells in the same cortical column to develop slightly different receptive fields, because both the probability of connection and its strength are random variables[26]. In this work, we did not simulate the whole model but only computed the mean receptive field at each location. We have previously shown the mean receptive field can be computed as a weighted sum of the afferent LGN input:

$$\Psi = \sum_i \exp\left(-d_i^2 / 2\bar{\sigma}^2\right) \cdot \Psi_i^{LGN}$$

where

$$\bar{\sigma} = \frac{\sigma_{\text{conn}} \cdot \sigma_{\text{syn}}}{\sqrt{\sigma_{\text{conn}}^2 + \sigma_{\text{syn}}^2}}$$

and where Ψ_i^{LGN} is the receptive field of the i^{th} LGN neuron and d_i is the distance between the locations of the LGN afferent and the cortical site where we are calculating the mean receptive field. The values of σ_{conn} and σ_{syn} were set as 25 μm of cortical space, and they represent the rates of the spatial falloff of the probabilities of connectivity and synaptic strength, respectively, which are assumed to be Gaussian. (See ref. 27 for a detailed description of these parameters and derivations.)

Cortical map measurements. After the mean receptive field was calculated at each cortical position, we estimated its preferred orientation and selectivity from its Fourier transform $\Psi(\omega)$ as follows. The preferred orientation is defined as $\theta_{pref} = \arg(\mu)/2$, where

$$\mu = \int |\Psi(\omega)|\,|\omega|\exp(2i\arg(\omega))d\omega \Big/ \int |\Psi(\omega)|\,d\omega.$$

Orientation selectivity index (OSI) was defined as

$$\text{OSI} = \frac{\left|\int |\Psi(\omega_{pref},\theta)|\exp(2i\theta)\,d\theta\right|}{\int |\Psi(\omega_{pref},\theta)|\,d\theta}$$

where $\omega_{pref} = |\mu|$ is the preferred spatial frequency of the receptive field filter.

Selectivity-weighted orientation map. The predicted OSI varies across the cortex and is maximal at locations where cortical sites receive input dominated from a single dipole. These strongly tuned sites contribute largely to the orientation tuning in the cortex, thus seeding the orientation map. To identify the location and preferred orientation angles of such signals, we sampled the cortical locations with an OSI higher than a specified threshold OSI > 0.25 (**Figs. 1d** and **2d** and **Supplementary Fig. 4**). For visualization, a smooth continuous version of the map is obtained by diffusion of orientations with a Gaussian window of 140 μm in cortical space. These smooth maps are shown in the right panels of **Figures 1d** and **2b** and **Supplementary Figure 4**.

Analysis of experimental orientation maps. Regions of interest (ROI) in the experimental maps were selected by avoiding areas that were too close to the V1/V2 boundary and having moderate size (~3 × 3 orientation periods). For each individual we chose between two and four non-overlapping ROIs. Selecting ROIs of intermediate size is important because locally the maps can have hexagonal structure, but over a long range the orientation of the structure can drift. In such a case, computing the autocorrelation of over a very large area can obliterate the secondary peaks observed in the autocorrelation function using smaller ROIs. Conversely, the smaller the ROI, the more likely we are to obtain peaks in the autocorrelation by mere chance. Thus, we adopted a strategy where we averaged the autocorrelation functions of non-overlapping ROIs for each individual after appropriate normalization (see **Supplementary Fig. 2**).

To compute the statistical significance of secondary peaks in the autocorrelation function, we calculated the probability that they could have resulted by chance from control orientation maps. These control maps were generated by enforcing their Fourier amplitude spectrum to be isotropic and having the same marginal, radial amplitude spectrum as the map under consideration (a detailed description of the method is provided in the **Supplementary Discussion** and **Supplementary Fig. 3**).

Orientation maps in cat are from ref. 49, and tree shrew and ferret data were provided by D. Fitzpatrick (Max Planck Florida Institute), with L. White, W. Bosking and Y. Li (personal communication). Orientation maps from monkey primary visual cortex were obtained from reference 50.

49. Benucci, A., Ringach, D.L. & Carandini, M. Coding of stimulus sequences by population responses in visual cortex. *Nat. Neurosci.* **12**, 1317–1324 (2009).
50. Blasdel, G.G. Orientation selectivity, preference, and continuity in monkey striate cortex. *J. Neurosci.* **12**, 3139–3161 (1992).

doi:10.1038/nn.2824

Synaptic Plasticity Controls Sensory Responses through Frequency-Dependent Gamma Oscillation Resonance

Se-Bum Paik[1]*, Donald A. Glaser[1,2]

1 Department of Physics, University of California Berkeley, Berkeley, California, United States of America, **2** Department of Molecular and Cell Biology, University of California Berkeley, Berkeley, California, United States of America

Abstract

Synchronized gamma frequency oscillations in neural networks are thought to be important to sensory information processing, and their effects have been intensively studied. Here we describe a mechanism by which the nervous system can readily control gamma oscillation effects, depending selectively on visual stimuli. Using a model neural network simulation, we found that sensory response in the primary visual cortex is significantly modulated by the resonance between "spontaneous" and "stimulus-driven" oscillations. This gamma resonance can be precisely controlled by the synaptic plasticity of thalamocortical connections, and cortical response is regulated differentially according to the resonance condition. The mechanism produces a selective synchronization between the afferent and downstream neural population. Our simulation results explain experimental observations such as stimulus-dependent synchronization between the thalamus and the cortex at different oscillation frequencies. The model generally shows how sensory information can be selectively routed depending on its frequency components.

Citation: Paik S-B, Glaser DA (2010) Synaptic Plasticity Controls Sensory Responses through Frequency-Dependent Gamma Oscillation Resonance. PLoS Comput Biol 6(9): e1000927. doi:10.1371/journal.pcbi.1000927

Editor: Karl J. Friston, University College London, United Kingdom

Received April 26, 2010; **Accepted** August 10, 2010; **Published** September 9, 2010

Funding: The authors received no funding for this work.

Competing Interests: The authors have declared that no competing interests exist.

* E-mail: spaik@berkeley.edu

Introduction

Synchronous oscillations [1–3] in neural networks are thought to be important to sensory and cognitive functions [4,5]. In particular, gamma band oscillations (30~70Hz) have been observed in various neural circuits [6,7], and their role has been intensively studied [8–11]. Gamma oscillations synchronize the response of neural populations [12], selectively amplify local sensory signals [13], enhance signal transmission by reducing noise [14], and regulate information processing by phase-dependent gating [15]. However, little is known about the mechanism by which the nervous system controls or takes advantage of these gamma oscillation effects. Here we suggest that sensory response can be precisely controlled by the synaptic plasticity of a neural circuit, through the dynamic modulation of spontaneous gamma oscillations. Using a model neural network of the primary visual cortex (V1), we show that (i) the resonance between spontaneous and stimulus-driven oscillations regulates sensory responses and synchrony in a neural population; (ii) the synaptic plasticity of thalamocortical neurons modulates the frequency of spontaneous oscillation in V1; and (iii) this change of spontaneous oscillation regulates gamma resonance, thus controlling the afferent-downstream synchrony. We found that this synaptic modulation can either facilitate or depress the response of the network to stimuli, by changing gamma resonance conditions. Our results suggest that the brain can readily control its synchrony condition for the proper processing of sensory information.

Results

Gamma oscillations in model neural network

We performed our simulations with a model cortical network of excitatory (E) and inhibitory (I) neurons (1mm by 1mm, consisting of 3341 neurons) adapted from our previous study [13] (Fig. 1A, top). When feedforward input spikes (generated by random Poisson process) were injected into the model visual cortex network, neurons generated spontaneous gamma rhythms in their firing pattern (Fig. 1B and C). The spontaneous oscillations were detectable almost whenever the connections between E and I cells were allowed and the input spike rate was above a certain level (~10spikes/s) that can drive a measurable amount of cortical responses (for detailed parameter tests, see ref. 13). As we reported previously, the frequency of oscillation was modulated by changes in the thalamocortical synaptic strength parameter that controls the excitatory postsynaptic conductance (EPSC) in cortical neurons induced by a feedforward input spike. In the first part of this study, we fixed this thalamocortical synaptic strength and examined the effect of temporal changes in input spike rate only. Subsequently we studied how variations in thalamocorical synaptic strength affect cortical responses.

Spontaneous and stimulus-driven oscillations

We first controlled input firing rate patterns to examine how gamma oscillation is regulated when feedforward input spike rate varies temporally (Fig. 1A, bottom). For static input, mean input firing rate was set to 40spike/s, and the input spike correlogram indicated no temporal correlation between input spikes (Fig. 1B). Responding to this input, cortical neurons generated an oscillatory output spikes pattern. The oscillation power spectrum showed one strong spontaneous gamma peak at $f^s_{out} = 38$Hz; inter-spike interval (ISI) distribution showed that most I cells fired in every gamma cycle, while E cells fired, on average, less than once in a cycle (Fig. 1D). In addition, I cells were synchronized more sharply than E cells in each gamma cycle, indicating that this gamma rhythm was induced by

Author Summary

In the nervous system, a network of neurons shows interesting population activities. One example is a various frequency of synchronized oscillations which are thought to be important to sensory functions. In particular, it has been reported that gamma frequency rhythms (30~70Hz) in the cortex can significantly regulate the responses to visual stimuli. In this study, we further investigate the mechanism by which the nervous system can control the effect of gamma oscillation on the modulation of neural responses. We found that the sensory response of the visual cortex strongly depends on the extent of synchronization between external stimulus rhythms and spontaneous gamma oscillations in the cortical network. Furthermore, the simulation results show that the plasticity of the neural circuit can modulate the frequency of spontaneous gamma oscillations, thus readily controlling neural population responsiveness. This finding is related to the question of how the brain efficiently interprets external input signals under various conditions, using its internal neural connectivity. Our study provides insight into this question.

fast-spiking I cells. For oscillating input, in contrast, we drove the network with sinusoidally oscillating input (mean firing rate 40 spikes/s, mean oscillation amplitude ±20 spikes/s), at the same frequency as the spontaneous gamma oscillation frequency for static input (f^s_{out}). In this instance, output oscillation frequency was the same as input frequency (Fig. 1E), but the correlation of output spikes became stronger, and the output rate pattern was phase-locked to input oscillation cycle (Fig. 1C). The ISI distributions of E and I cells were also sharpened, showing that the "gating" or "temporal sharpening" effect [15] of sensory responses is enhanced by coherent input oscillations [16,17] (Fig. 1E). We refer to this modulation as "resonance" between spontaneous and stimulus-driven oscillations.

Stimulus-driven oscillations: Input frequency variation

To further examine the resonance condition between spontaneous and driven oscillations, we injected various frequencies of oscillating inputs to the network. Input frequency was varied within the range $f_{in} = 25 \sim 55$Hz, similar to the boundary of spontaneous oscillation frequency observed in our previous study [13]. When f_{in} was markedly different from the spontaneous oscillation frequency ($f^s_{out} = 38$Hz) for static input, the network displayed two separate peaks in its spectrum (Fig. 2A, red and blue arrows), showing that two different types of oscillations coexist in the cortical response. The spontaneous oscillation peak (blue arrows) remained the same (38Hz) but became weaker than in the previous cases (Fig. 1D, E). The driven oscillation peak (red arrows) appeared at f_{in}, confirming that this oscillation was driven by the input spikes pattern. Thus, in this case, spontaneous and driven oscillations existed independently. In contrast, when f_{in} was relatively close but not identical to f^s_{out}, the spontaneous oscillation peak at f^s_{out} disappeared, and the power spectrum displayed only one peak near f_{in} (Fig. 2A, purple arrows), demonstrating the

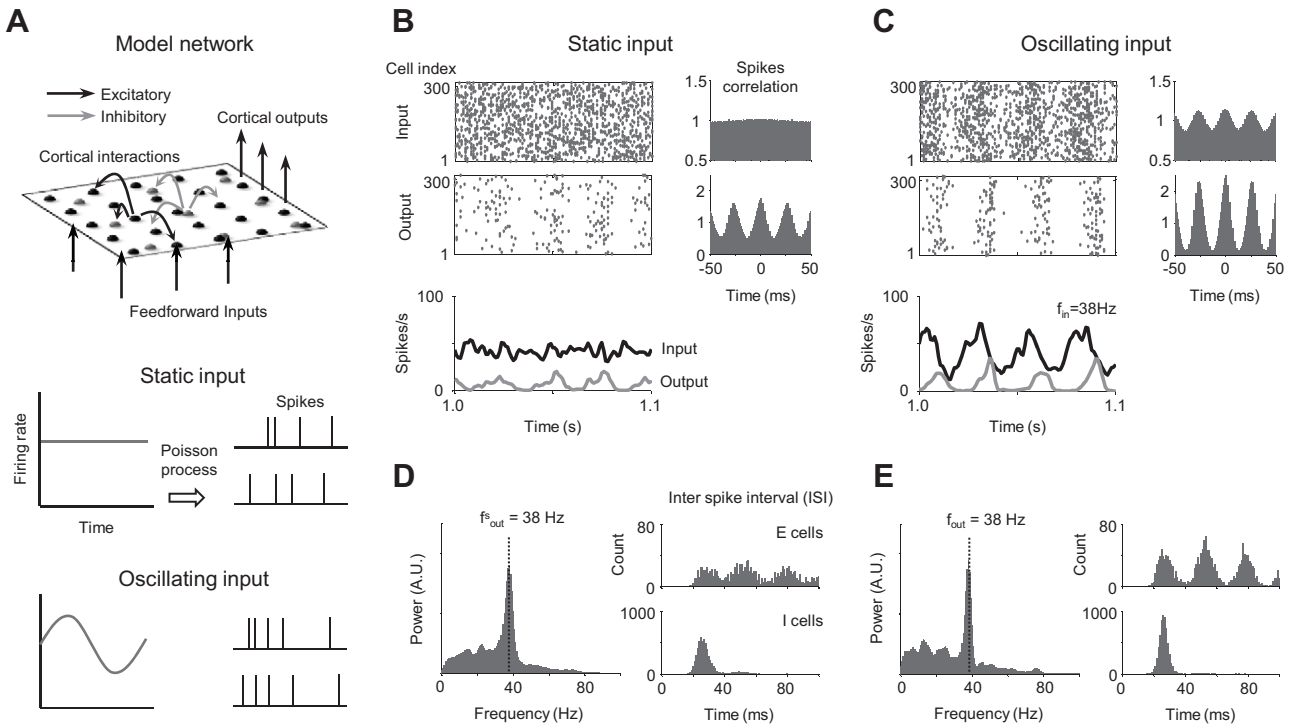

Figure 1. Synchronized population response to static and oscillating inputs. (A) The model visual cortex network. Each excitatory (E) and inhibitory (I) cell receives feedforward inputs from the thalamus, and cortical inputs from the other E and I cells within the range of lateral connections. (B) Population firing rates and spike correlograms for static input and (C) for sinusoidally oscillating input at 38Hz. Correlograms were normalized so that the uncorrelated state is set to unity. (D) Oscillation power spectrum of population firing rate and inter-spike interval (ISI) distribution for static input and (E) for oscillating input. Note that ISI distribution is sharper in (E) than (D), even though gamma oscillation frequencies are the same. For oscillation power spectrum, only the E cells result is displayed, because E and I populations showed identical peak distributions.
doi:10.1371/journal.pcbi.1000927.g001

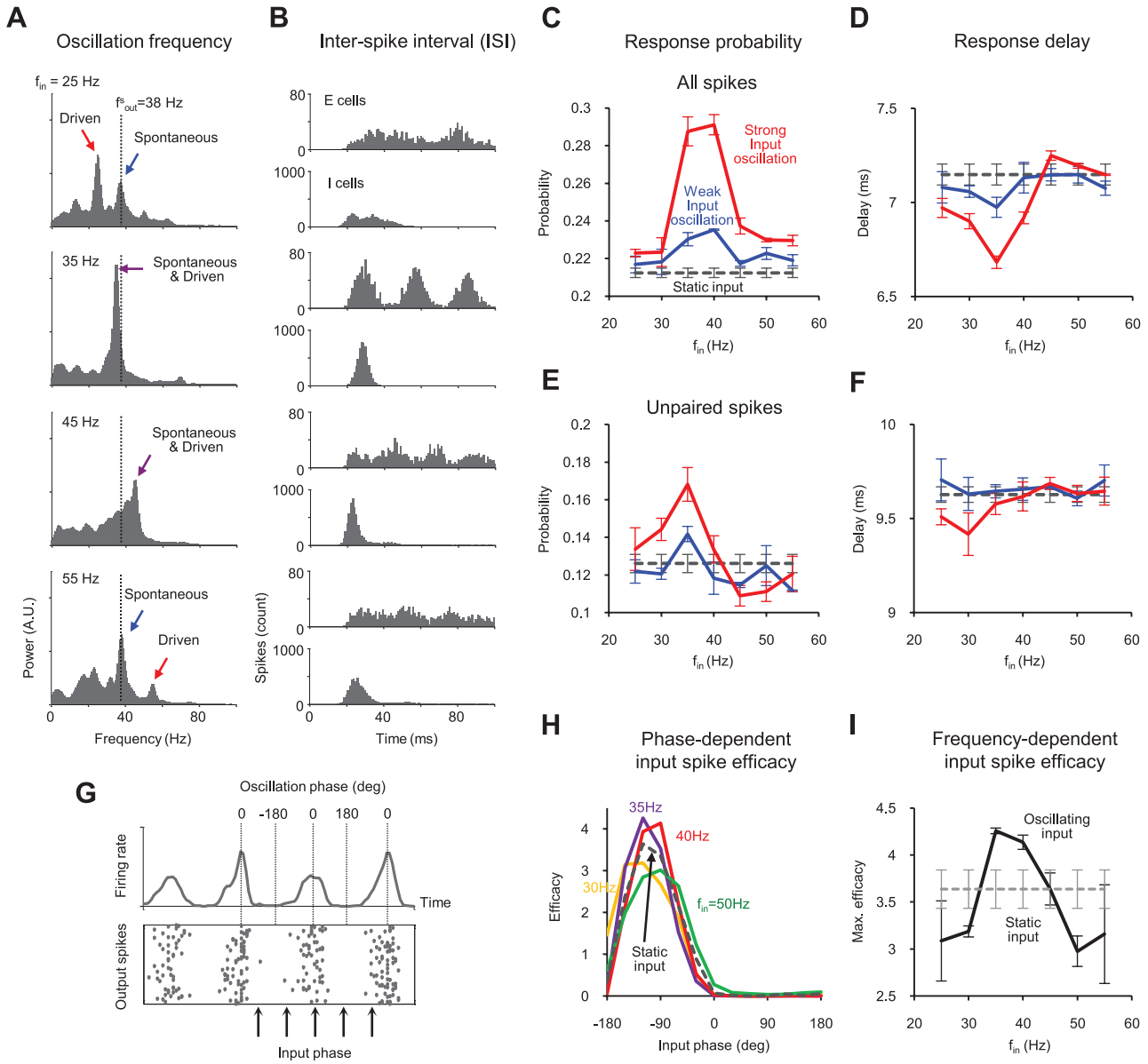

Figure 2. Population response modulation by the resonance between spontaneous and driven gamma oscillations. (A) Cortical output oscillation power spectrum and (B) ISI distributions for sinusoidally oscillating inputs. Note that the resonance between spontaneous and driven oscillations occurs only when input frequency (f_{in}) is close to spontaneous gamma frequency (f^{s}_{out}). (C) Response probability and (D) Response delay to all input spikes of various oscillation frequencies. (E) Response probability and (F) Response delay to temporally "unpaired" input spikes. (G) Relative input timing (phase) in a gamma oscillation cycle. (H) Variation of input spike efficacy by input phase. The efficacy of unpaired input spikes was defined as the relative probability to generate cortical spike, and was measured as a function of input phase. The efficacy was normalized so that the average of each set was set to unity. (I) Maximum input spike efficacy in (H). This shows the network's ability to "gate" or synchronize its output signals.
doi:10.1371/journal.pcbi.1000927.g002

resonance between spontaneous and driven oscillations. In addition, ISI distributions became sharper than in "irresonant" cases (Fig. 2B). Therefore, when f_{in} is close enough to f^{s}_{out}, spontaneous oscillation frequency is adjusted close to driven oscillation frequency, and the resonance between two oscillations strengthens cortical gamma rhythm, which enhances the synchronization of cortical spike activities.

Responsiveness modulation by frequency-dependent gamma resonances

Next, we examined how cortical responsiveness is modulated by gamma oscillation resonance. We varied input frequencies ($f_{in} = 25 \sim 55$Hz) for different input oscillation strengths. The oscillation amplitude of the input spike rate was set to ± 10 spikes/s for weak oscillation and ± 20 spikes/s for strong oscillation; mean input rate was 40 spikes/s for all static and oscillating inputs. We measured the output spike probability to a single input spike as the response probability [13] of the cortical neurons. When f_{in} was close to spontaneous oscillation frequency ($f^{s}_{out} = 38$Hz), where the gamma oscillation resonance was strong, response probability was significantly enhanced (Fig. 2C), and response delay was decreased (Fig. 2D). Response modulations were larger for the stronger oscillation. We further investigated whether these modulations might have resulted from temporal

correlation changes in the input spike pattern [18], simply due to input frequency variation. In order to remove any influence from input correlation, we sampled temporally "unpaired" input spikes and again measured cortical responses to them. Input spikes were chosen only if there were no other input spikes within 20ms before and after in the same neuron. Even in this case, the response probability was noticeably higher around the gamma resonance area (Fig. 2E), confirming a significant change in cortical responsiveness. However, response delay did not change as much as in the previous result (Fig. 2F), suggesting that this value strongly depends on the temporal correlation of input spikes.

We also examined the dependence of response modulation on the oscillation phase in each cycle. A normalized efficacy of each unpaired input spike was defined as a relative probability to generate a cortical spike, and was measured as a function of input spike phase (Fig. 2G) in each gamma cycle. In Fig. 2H, the input spike efficacy plot shows a "pass" band before 0° phase with a peak value around -90°, and a "block" band after 0° phase, which is known as the mechanism of temporal regulation (or selective gating) of sensory signals in gamma oscillation [15]. In other words, input spikes within the pass band phase have a much higher probability of generating cortical spikes than those within the block band. We found that the pass band was sharpened by gamma resonance. During resonance, the pass band amplitude grew higher and the width narrowed (Fig. 2H, $f_{in} = 35$Hz and 40Hz). The increase of the maximum in the normalized efficacy means that the pass band is sharpened by gamma resonance (Fig. 2I). As a result, the network's ability to synchronize cortical responses was enhanced by gamma resonance. This result suggests that sensory responses can be manipulated by controlling gamma resonance.

Spontaneous gamma oscillation frequency modulation by synaptic plasticity

It was previously reported that the frequency of gamma oscillation can be rapidly modulated by instantaneous changes in synaptic excitation-inhibition balance [13,19,20]. Based on these findings, we hypothesized that the synaptic plasticity of thalamocortical connections can control the frequency of spontaneous cortical gamma oscillation, and therefore regulate sensory responses. To test this idea, we first examined how the frequency of spontaneous cortical oscillation was regulated by the change of thalamocortical synaptic strength. In our simulations, we controlled the amplitude (g_{max}) of EPSC driven by each input spike, as a simulation of the synaptic plasticity of LGN-V1 connections (Fig. 3A). We confirmed that the frequency of spontaneous cortical gamma oscillation (f^s_{out}) increased as g_{max} increased (Fig. 3B), a conclusion that was qualitatively observed in our previous simulations [13]. This frequency variation can be explained by the modulation of synaptic excitation-inhibition [19,20] and response delay [13]. In our simulations, f^s_{out} varied from 37Hz to 61Hz (Fig. 3C).

Resonance modulation by synaptic plasticity

Based on these results, we assumed that selective response regulation (depending on input pattern) can be achieved by synaptic plasticity through the control of gamma oscillation resonance, because the resonance frequency of the system is shifted by the changes in g_{max}. To further test this assumption, we varied g_{max} under different input frequencies ($f_{in} = 40$, 45, 50Hz) and measured the response probability of the network (Fig. 4A). As we expected, response probability increased near the gamma resonance region, but the resonance point changed noticeably depending on input frequency. For example, when $f_{in} = 40$Hz, the response enhancement was largest at $g_{max} = 40\mu S/cm^2$, where g_{max} corresponds to

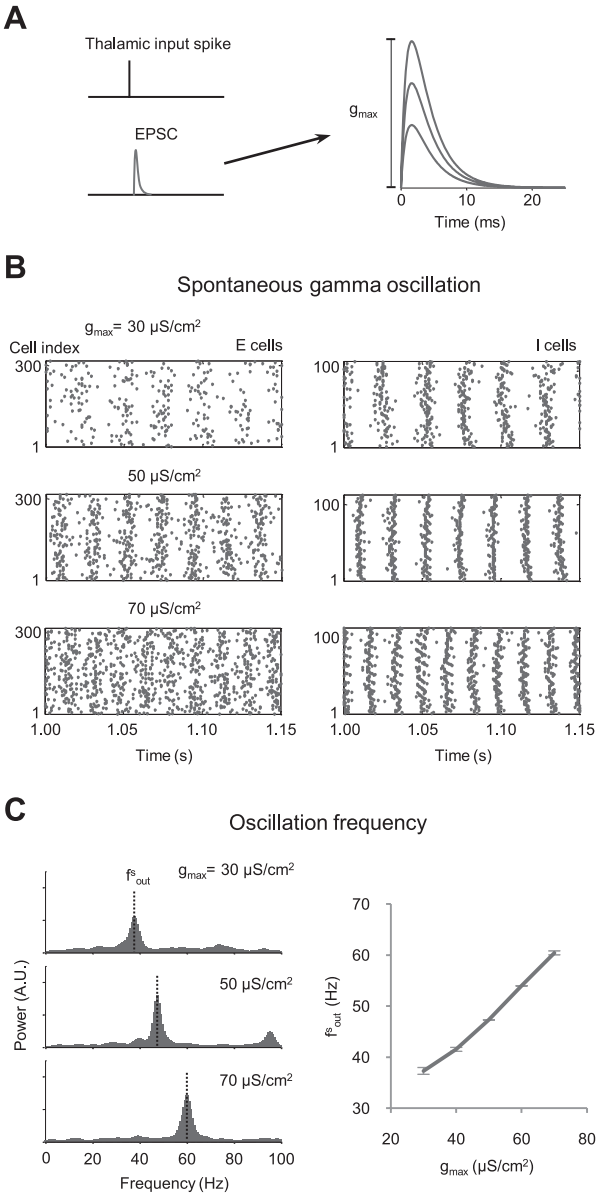

Figure 3. Control of gamma oscillation by synaptic plasticity. (A) The amplitude (g_{max}) of excitatory postsynaptic conductance (EPSC) by thalamocortical input spikes is controlled as a simulation of synaptic plasticity. (B) Spontaneous synchrony in the spike firings of E and I cells for various g_{max}. (C) Spontaneous gamma oscillation frequency modulation by synaptic plasticity.
doi:10.1371/journal.pcbi.1000927.g003

spontaneous oscillation frequency $f^s_{out} \sim 40$Hz (Fig. 3C). When $f_{in} = 50$Hz, the resonance point shifted to $g_{max} = 60\mu S/cm^2$, where f^s_{out} is close to 50Hz. The response delay of cortical neurons was similarly modulated (Fig. 4B). Gamma resonance thus occurs at different points, depending on input frequency, f_{in}, and the amplitude of EPSC, g_{max}. In other words, when g_{max} is changed through synaptic plasticity, gamma oscillation regulates the cortical network response selectively, depending on f_{in}.

Discussion

We have shown that sensory responses can be facilitated or depressed, depending on the resonance condition between

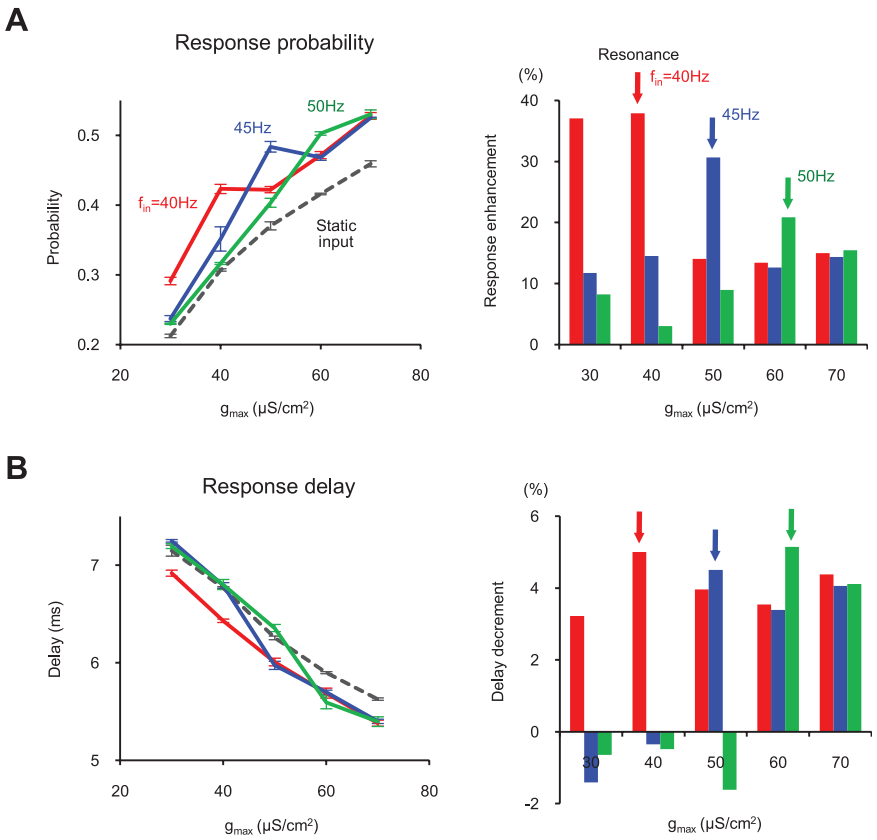

Figure 4. Gamma oscillation resonance tuning by synaptic plasticity. (A) Response probability modulation by frequency-dependent gamma resonance. Response enhancement was defined as the difference between the responses to static input and to other inputs. Note that the peak value of modulation (resonance point) varies by input frequency. (B) Response delay modulation. Negative values in response delay decrement mean increased delay.
doi:10.1371/journal.pcbi.1000927.g004

spontaneous and driven oscillations in the cortex. Here we discuss previous experimental observations that are relevant to our findings. We demonstrate that these experimental results can be explained by our model. We also discuss possible mechanisms by which thalamocortical synaptic plasticity can be controlled by the variation of visual stimuli, which enables the proper modulation of the gamma oscillation resonance and the afferent-downstream synchronization.

Synchronization between the feedforward and cortical oscillation

Synchronized oscillations of various frequencies are observed in the visual pathway [21–23] and are thought to convey information about the visual scene [5,24]. Previously, Castelo-Branco and colleagues reported a strong correlation of oscillatory responses between the retina, LGN, and the visual cortex in an anesthetized cat [25]. Their observations are in good agreement with our model.

First, cortical oscillation frequencies are clustered as two distinct bands (low-frequency 30–60Hz, high-frequency 60–120Hz). These low- and high- frequency oscillations can coexist in the cortex. High-frequency oscillations in the cortex are shown to be the result of feedforward synchronization with the retina and LGN activity whose oscillation frequencies are in this range. Low-frequency oscillations are shown to be spontaneous gamma oscillations in the cortical circuit. In our model simulation, cortical spikes could be driven by feedforward oscillations of various frequencies, from above spontaneous gamma frequency to over 120Hz (not shown here). Therefore, as shown in our results, cortical responses can be synchronized by two different activities: spontaneous and driven oscillations.

Second, cortical oscillation frequency strongly depends on stimulus condition. For stationary stimuli, cortical neurons are synchronized with high frequency (60–120 Hz) feedforward oscillations. For dynamic stimuli, slow cortical oscillations (30–60Hz) dominate, and subcortical high frequency oscillations become transient. In our model, these two cases are different "resonance" modes; the mode can switch, depending on whether the resonant point is closer to low-frequency cortical gamma oscillation or high-frequency feedforward oscillation. Since the temporal correlation of a feedforward spike train can vary according to stimulus condition, thalmocortical synaptic strength can be modified by activity-dependent short-term plasticity [26]. If this modification arises differently for two stimuli types, the observed variation of cortical oscillation frequency is readily explained. The strengthened synapses increase spontaneous cortical gamma oscillation frequency, resulting in cortical synchronization with the high-frequency feedforward oscillations. On the other hand, if thalamocortical synapses don't change, low-frequency spontaneous gamma oscillations dominate, and the feedforward oscillation becomes transient. As a result of this stimulus-specific synchronization mechanism, cortical activity can be tuned to various oscillation frequencies.

When cortical spontaneous oscillations are strong, LGN activity can be synchronized to cortical oscillations with a retarded phase. Because this situation requires a corticothalamic feedback loop [25], it cannot be fully described by our current model. Generally, this feedback is assumed as a mechanism of population activity normalization or gain control [27]. In our model, the addition of a corticothalamic feedback loop could work as another possible controller of thalamocortical synaptic strength. This mechanism will be further studied in future work.

Another relevant example is that information in the hippocampus is differentially routed, depending on its fast and slow gamma frequency components [28]. This might be a slightly different version of the above mechanism, and we suggest that our gamma resonance model can be a promising candidate for this type of input-specific neuronal synchronization.

Dynamic resonance tuning by short-term plasticity

Short-term synaptic plasticity [26,29] has been observed at various places in the nervous system and is thought to be important to the precise tuning of sensory responses depending on stimuli conditions [30,31]. At the thalamocortical synapses of the somatosensory system, plasticity usually appears as a form of short-term depression [32–34]. Similar thalamocortical synaptic depression is also found in the visual system of the cat in vitro [35,36] and in vivo [37]. However, the effect of thalamocortical synaptic plasticity on visual cortex response is still open to question, because it seems to work both ways: the cortical response can be either depressed or facilitated [18,38,39].

From the observations above, it seems possible that stimuli-dependent short-term plasticity at the thalamocortical synapse controls the resonance between feedforward and cortical activities. Rapid changes in synaptic excitation can modulate the frequency and amplitude of gamma oscillations of a neural network [19]. In our simulations, spontaneous gamma frequency varied from 37Hz to 61Hz, which is comparable to measured gamma peak frequency variation in humans [40] caused by excitation-inhibition balance modulation. Since oscillation frequency changes very rapidly in this way, cortical activity can be modulated cycle-by-cycle in gamma rhythms. Thus it can be an effective method of regulating dynamic sensory response to rapidly varying stimuli. In addition, the gamma modulation effect can be spatially localized fairly tightly: a small neural population can be tuned selectively by well-localized feedforward inputs [13]. In this way, a neural network can suitably control its sensory response to complicated (spatially and temporally) visual stimuli patterns.

Oscillation resonance and long-term plasticity

Although there is no direct experimental evidence yet, it is also possible to relate our model to developing visual systems in young animals, as a tuning mechanism of thalamocortical and corticothalamic synaptic strength. In this case, long-term plasticity [41] becomes important. Long-term potentiation and depression (LTP and LTD) are observed at thalamocortical synapses in the developing somatosensory cortex [42] and visual cortex [43] and are thought to contribute to the stimulus-dependent enhancement of sensory responses. As with the short-term plasticity described above, activity-dependent synaptic plasticity can differentially tune the thalamocortical circuit, depending on the stimulus condition. As a result, the resonance between feedforward and cortical oscillations is modified accordingly, which may contribute to the experience-dependent development of the sensory system. For example, if thalamocortical EPSC varies differentially depending on the visual stimulus pattern by spike timing dependent plasticity (STDP) [44,45], this will change spontaneous cortical oscillation frequency. LGN-cortex resonance, accordingly, will alternate between two modes: "resonance" and "irresonance." An experimental observation that cortical plasticity can be driven by different thalamic activity patterns [46] also suggests the possibility of such a resonance control mechanism. Recently it was shown that a single neuron equipped with STDP can robustly detect input spike patterns [47], and that this downstream learning is noticeably facilitated by oscillatory drive with "phase-of-firing coding (PoFC)." Considering that synchronized oscillations are commonly observed in the visual pathway [21–23], thalamocortical synapses might be properly learned by oscillations in an earlier pathway, or by activities in the corticothalamic feedback loop.

In conclusion, we demonstrate that the resonance between spontaneous and driven gamma oscillations can significantly regulate sensory responses in a neural population. The synaptic plasticity of thalamocortical neurons can readily control gamma resonance by varying the frequency of spontaneous oscillation, and therefore can selectively enhance or degrade the network's processing of information. Our results suggest a general model of how the nervous system can make use of its internal plasticity for the effective control of sensory responses under various conditions. The simplicity and the wide applicability of our model make it a serious candidate for further experimental tests.

Methods

Network model

A two-dimensional layer model of the cortex neural network was used in our simulations, slightly adapted from our previous work [13]. The network size is 1mm by 1mm, including 3341 neurons. The network consists of simplified E (75%) and I (25%) model neurons with Hodgkin-Huxley type Na^+ and K^+ ion channels and synaptic conductance channels.

The membrane potential of an individual neuron, v, is determined by $C(dv/dt) = -g_L(v-V_L) - G_{Na}(v-V_{Na}) - G_K(v-V_K) - g_{\sigma E}(t)(v-V_E) - g_{\sigma I}(t)(v-V_I) - g_{input}(t)(v-V_E)$, where σ is the type of neuron (E or I), C is the membrane capacitance, and g_L is the leakage conductance. $g_{\sigma E}$ and $g_{\sigma I}$ are the synaptic conductances, providing the cortical E and I inputs. We used the commonly accepted values for physiological parameters ($C = 10^{-6}$ Fcm^{-2}, $V_L = -70$mV, $V_{Na} = 55$mV, $V_K = -80$mV, $V_E = 0$mV, $V_I = -80$mV and $g_L = 50*10^{-6}$ Scm^{-2}). The Hodgkin-Huxley ion channel conductance G_{Na} and G_K takes the generally known form [48,49] as in our previous work [13].

We have assumed spatially isotropic local cortico-cortical connections. A neuron's synaptic conductance is given by $g_{\sigma E}(t) = W_{\sigma E}\sum_r \Delta^r_{\sigma E}\sum_{t'} G_E(t-t')$, $g_{\sigma I}(t) = W_{\sigma I}\sum_r \Delta^r_{\sigma I}\sum_{t'} G_I(t-t')$, where t's are input spike timings. The spatial connection factor takes the form $\Delta^r_{\sigma\sigma'} = \exp(-r/\lambda_{\sigma'})$, where r is the cortical distance, and σ and σ' are the type of connected neurons (E or I). The spatial connection decay constants were set as $\lambda_E = 200\mu$m, $\lambda_I = 100\mu$m. The excitatory and inhibitory postsynaptic conductance fluctuations were set as $G_\sigma(t) = [\exp(-t/\tau_1) - \exp(-t/\tau_2)]/(\tau_1 - \tau_2)$. The time constants (τ_1, τ_2) in milliseconds were set as (3, 1) for σ = E and (7, 1) for σ = I. The contribution of each cortical interaction was controlled by weighting factor $W_{\sigma\sigma'}$ for the type of neuron pair (σ, σ').

The EPSC driven by thalamocortical feedforward input spikes was given by $g_{input}(t) = g_{\max}\sum_{t'} G_E(t-t')$. $g_{\max}$ sets the maximum fluctuation amplitude and was varied within 30~70 μS/cm^2 as a simulation of synaptic plasticity.

Simulation and data analysis

Our simulations were performed using the GENESIS 2.3 environment (Text S1) [49]. Simulation outputs were analyzed using Matlab scripts.

Supporting Information

Text S1 GENESIS simulator configuration: A two-dimensional model neural network.

Found at: doi:10.1371/journal.pcbi.1000927.s001 (0.11 MB PDF)

Author Contributions

Conceived and designed the experiments: SBP DAG. Performed the experiments: SBP. Analyzed the data: SBP. Wrote the paper: SBP DAG.

References

1. Gray CM (1994) Synchronous oscillations in neuronal systems: mechanisms and functions. J Comput Neurosci 1: 11–38.
2. Salinas E, Sejnowski TJ (2001) Correlated neuronal activity and the flow of neural information. Nat Rev Neurosci 2: 539–550.
3. Steriade M (2006) Grouping of brain rhythms in corticothalamic systems. Neuroscience 137: 1087–1106.
4. Schoffelen JM, Oostenveld R, Fries P (2005) Neuronal coherence as a mechanism of effective corticospinal interaction. Science 308: 111–113.
5. Koepsell K, Sommer FT (2008) Information transmission in oscillatory neural activity. Biol Cybern 99: 403–416.
6. Whittington MA, Traub RD, Kopell N, Ermentrout B, Buhl EH (2000) Inhibition-based rhythms: experimental and mathematical observations on network dynamics. Int J Psychophysiol 38: 315–336.
7. Fries P, Nikolić D, Singer W (2007) The gamma cycle. Trends Neurosci 30: 309–316.
8. Whittington MA, Traub RD, Jefferys JGR (1995) Synchronized oscillations in interneuron networks driven by metabotropic glutamate receptor activation. Nature 373: 612–615.
9. Traub RD, Whittington MA, Stanford IM, Jefferys JGR (1996) A mechanism for generation of long-range synchronous fast oscillations in the cortex. Nature 383: 621–624.
10. Bögers C, Epstein S, Kopell NJ (2005) Background gamma rhythmicity and attention in cortical local circuits: a computational study. Proc Natl Acad Sci USA 102: 7002–7007.
11. Bartos M, Vida I, Jonas P (2007) Synaptic mechanisms of synchronized gamma oscillations in inhibitory interneuron networks. Nat Rev Neurosci 8: 45–56.
12. Fries P, Neuenschwander S, Engel AK, Goebel R, Singer W (2001) Rapid feature selective neuronal synchronization through correlated latency shifting. Nat Neurosci 4: 194–200.
13. Paik S, Kumar T, Glaser DA (2009) Spontaneous local gamma oscillation selectively enhances neural network responsiveness. PLoS Comp Biol 5: e1000342.
14. Sohal VS, Zhang F, Yizhar O, Deisseroth K (2009) Parvalbumin neurons and gamma rhythms enhance cortical circuit performance. Nature 459: 698–702.
15. Cardin JA, Carlen M, Meletis K, Knoblich U, Zhang F, et al. (2009) Driving fast-spiking cells induces gamma rhythm and controls sensory responses. Nature 459: 663–667.
16. Womelsdorf T, Schoffelen JM, Oostenveld R, Singer W, Desimone R, et al. (2007) Modulation of neuronal interactions through neuronal synchronization. Science 316: 1609–1612.
17. Popescu AT, Popa D, Pare D (2009) Coherent gamma oscillations couple the amygdale and striatum during learning. Nat Neurosci 12: 801–807.
18. Usrey WM, Alonso J, Reid RC (2000) Synaptic interactions between thalamic inputs to simple cells in cat visual cortex. J Neurosci 20: 5461–5467.
19. Atallah BV, Scanziani M (2009) Instantaneous modulation of gamma oscillation frequency by balancing excitation with inhibition. Neuron 62: 566–577.
20. Mann EO, Mody I (2010) Control of hippocampal gamma oscillation frequency by tonic inhibition and excitation of interneurons. Nat Neurosci 13: 205–212.
21. Laufer M, Verzeano M (1967) Periodic activity in the visual system of the cat. Vis Res 7: 215–229.
22. Neuenschwander S, Singer W (1996) Long-range synchronization of oscillatory light responses in the cat retina and lateral geniculate nucleus. Nature 379: 728–733.
23. Hughes SW, Lorincz M, Cope DW, Blethyn KL, Kekesi KA, et al. (2004) Synchronized oscillations at α and θ frequencies in the lateral geniculate nucleus. Neuron, 42: 253–268.
24. Koepsell K, Wang X, Vaingankar V, Wei Y, Wang Q, et al. (2009) Retinal oscillations carry visual information to cortex. Front Syst Neurosci 4: 1–18.
25. Castelo-Branco M, Neuenschwander S, Singer W (1998) Synchronization of visual responses between the cortex, lateral geniculate nucleus, and retina in the anesthetized cat. J Neurosci 18: 6395–6410.
26. Zucker RS (1999) Calcium- and activity-dependent synaptic plasticity. Curr Opin Neurobiol 9: 305–313.
27. Ringach DL (2010) Population coding under normalization. Vision Res (in press).
28. Colgin LL, Denninger T, Fyhn M, Hafting T, Bonnevie T, et al. (2009) Frequency of gamma oscillations routes flow of information in the hippocampus. Nature 462: 353–357.
29. Dobrunz LE, Huang EP, Stevens CF (1997) Very short-term plasticity in hippocampal synapses. Proc Natl Acad Sci USA 94: 14843–14847.
30. Chance FS, Nelson SB, Abbott LF (1998) Synaptic depression and the temporal response characteristics of V1 cells. J Neurosci 18: 4785–4799.
31. Bannister NJ, Nelson JC, Jack JJ (2002) Excitatory inputs to spiny cells in layers 4 and 6 of cat striate cortex. Philos Trans R Soc Lond B Biol Sci 357: 1793–1808.
32. Castro-Alamancos MA (2002) Different temporal processing of sensory inputs in the rat thalamus during quiescent and information processing states in vivo. J Physiol (Lond) 539: 567–578.
33. Chung S, Li X, Nelson SB (2002) Short-term depression at thalamocortical synapses contributes to rapid adaptation of cortical sensory responses in vivo. Neuron 34: 437–446.
34. Swadlow HA, Gusev AG, Bezdudnaya T (2002) Activation of a cortical column by a thalamocortical impulse. J Neurosci 22: 7766–7773.
35. Stratford KJ, Tarczy-Hornoch K, Martin KA, Bannister NJ, Jack JJ (1996) Intracortical excitation of spiny neurons in layer 4 of cat striate cortex in vitro. Cereb Cortex 9: 833–843.
36. Bannister NJ, Nelson JC, Jack JJ (2002) Excitatory inputs to spiny cells in layers 4 and 6 of cat striate cortex. Philos Trans R Soc Lond B Biol Sci 357: 1793–1808.
37. Boudreau CE, Ferster D (2005) Short-term depression in thalamocortical synapses of cat primary visual cortex. J Neurosci 25: 7179–7190.
38. Kara P, Pezaris JS, Yurgenson S, Reid RC (2002) The spatial receptive field of thalamic inputs to single cortical simple cells revealed by the interaction of visual and electrical stimulation. Proc Natl Acad Sci USA 99: 16261–16266.
39. Jia F, Xie X, Zhou Y (2004) Short-term depression of synaptic transmission from rat lateral geniculate nucleus to primary visual cortex in vivo. Brain Res 1002: 158–161.
40. Muthukumaraswamy SD, Edden RAE, Jones DK, Swettenham JB, Singh KD (2009) Resting GABA concentration predicts peak gamma frequency and fMRI amplitude in response to visual stimulation in humans. Proc Natl Acad Sci U S A 106: 8356–8361.
41. Bliss TVP, Collingridge GL (1993) A synaptic model of memory: long-term potnetiation in the hippocampus. Nature 361: 31–39.
42. Feldman DE, Nicoll RA, Malenka RC (1999) Synaptic plasticity at thalamocortical synapses in developing rat somatosensory cortex: LTP, LTD, and silent synapses. J Neurobiol 41: 92–101.
43. Yoshimura Y, Inaba M, Yamada K, Kurotani T, Begum T, et al. (2008) Involvement of T-type Ca2+ channels in the potentiation of synaptic and visual responses during the critical period in rat visual cortex. Eur J Neurosci 28: 730–743.
44. Dan Y, Poo M (2004) Spike timing-dependent plasticity of neural circuits. Neuron 44: 23–30.
45. Caporale N, Dan Y (2008) Spike timing-dependent plasticity: a hebbian learning rule. Annu Rev Neurosci 31: 25–46.
46. Linden ML, Heynen AJ, Haslinger RH, Bear MF (2009) Thalamic activity that drives visual cortical plasticity. Nat Neurosci 12: 390–392.
47. Masquelier T, Hugues E, Deco G, Thorpe SJ (2009) Oscillations, phase-of-firing coding, and spike timing-dependent plasticity: an efficient learning scheme. J Neurosci 29: 13484–13493.
48. Hodgkin A, Huxley A (1952) A quantitative description of membrane current and its application to conduction and excitation in nerve. J Physiol (London) 117: 500–544.
49. Bower J, Beeman D (2003) The Book of Genesis, Internet Edition. pp 44–47.

Link between orientation and retinotopic maps in primary visual cortex

Se-Bum Paik[a] and Dario L. Ringach[a,b,1]

[a]Department of Neurobiology, David Geffen School of Medicine, and [b]Department of Psychology, University of California, Los Angeles, CA 90095

Edited by Robert H. Wurtz, National Institutes of Health, Bethesda, MD, and approved March 19, 2012 (received for review November 17, 2011)

Maps representing the preference of neurons for the location and orientation of a stimulus on the visual field are a hallmark of primary visual cortex. It is not yet known how these maps develop and what function they play in visual processing. One hypothesis postulates that orientation maps are initially seeded by the spatial interference of ON- and OFF-center retinal receptive field mosaics. Here we show that such a mechanism predicts a link between the layout of orientation preferences around singularities of different signs and the cardinal axes of the retinotopic map. Moreover, we confirm the predicted relationship holds in tree shrew primary visual cortex. These findings provide additional support for the notion that spatially structured input from the retina may provide a blueprint for the early development of cortical maps and receptive fields. More broadly, it raises the possibility that spatially structured input from the periphery may shape the organization of primary sensory cortex of other modalities as well.

retinotopy | visuotopic map | pinwheel | statistical wiring | haphazard wiring

Sensory cortex is organized into vertical columns of neurons sharing similar preferences for stimulus properties (1, 2). The preference of neurons across the cortical surface can be represented as a map assigning each cortical site a set of preferred stimulus parameters. Two salient structures are normally observed in primary visual cortex of higher mammals: a retinotopic map, which assigns each location on the cortical surface a point in visual space, and an orientation map, which assigns each cortical site a preferred stimulus orientation (3–7). How these maps are established during development, how they relate to each other, and what function they play in normal visual processing remain fundamental, open questions in visual neuroscience (8–13).

Building on earlier work (14, 15), we have recently proposed that orientation maps may be established initially by the interference pattern of ON- and OFF-center, quasi-periodic retinal mosaics (16). Normal visual experience and activity-dependent synaptic learning can subsequently help maintain and refine this initial organization. Some of the model's predictions take the form of relationships between different maps, such as those for orientation, spatial frequency, and visual space (8). Under normal developmental conditions orientation maps in the adult are very similar to the earliest ones one can measure (17). Thus, we reasoned robust map properties predicted by the seeding mechanism might be detectable in the adult. Indeed, previous work has shown that the predicted hexagonal structure of the interference pattern is reflected in the organization of the orientation map (16, 18). Here we use the model to derive a peculiar prediction relating orientation and retinotopic maps and confirm that it holds in tree shrew primary visual cortex.

Results

Spatial Interference Model. We first consider an ideal version of the model, which helps develop an intuition for how the link between the maps come about. Suppose the receptive fields of ON-center and OFF-center retinal ganglion cells (RGCs) of a given class lie at the vertices of a perfect hexagonal grid (16). When two such patterns, having slightly different periodicities and orientations, are superimposed, the result is a periodic interference pattern (Fig. 1*A*). The period of the interference pattern depends on the ratio between periods of the component lattices and their relative orientation (16). An important property of the interference pattern is that the nearest neighbor of an ON-center cell is an OFF-center cell and vice versa. Thus, one may consider the interference pattern as composed of ON/OFF pairs or dipoles (15, 16). Our hypothesis is that in the early stages of development cortical cells have inputs dominated by individual dipoles that generate orientation-tuned receptive fields with side-by-side subregions of opposite sign (8, 16, 19) (Fig. 1*A*, *Lower*). Orientation dipoles systematically change their orientation over space, generating a blueprint for the orientation map (Fig. 1 *B* and *C*).

Predicted Link Between Orientation and Retinotopic Maps. The model generates an orientation map with a global structure that depends on the relative orientation between ON and OFF mosaics (16) (Fig. S1). We concentrate our discussion on the case when the relative orientation is zero. Other values of the relative orientation produce similar results (*SI Methods*).

When the relative angle between the RGC mosaics is zero, the resulting dipole orientations align along concentric circles centered on negative orientation singularities, with winding number −2, where orientation rotates clockwise two full cycles as one circumvents the singularity in a clockwise direction (Fig. 1*B*, *Lower Left* dipole pattern). Positive singularities, with winding number +1, where orientation rotates counterclockwise one cycle as one circumvents the singularity in a clockwise direction, are located equidistant from neighboring negative singularities (Fig. 1*B*, *Lower Right* dipole pattern). Both types of singularities occur at the vertices of hexagonal lattices (Fig. 1*B*, red and blue squares). The density of +1 singularities is twice that of −2 singularities, making the average topological sign over large areas equal to zero. A simulation of the full model based on such input gives rise to a smooth orientation map that reflects the basic organization of the dipoles (Fig. 1*C*) (16).

Consider now a local coordinate system aligned with the main retinotopic axes at the center of an orientation singularity (Fig. 1*D*). Each cortical site within its neighborhood can be assigned two angles, one representing the preferred orientation of the cortical column at that location, θ, and the other representing its angular displacement with respect to the horizontal meridian, ϕ. In what follows, we first focus our analysis on the distribution of angular differences $\theta - \phi$ (modulus 180°) at orientation singularities and consider their joint distribution later.

The model predicts that angular-difference distributions at singularities of opposite signs should have disparate shapes. In the

Author contributions: D.L.R. and S.-B.P. designed research, performed research, analyzed data, and wrote the paper.

The authors declare no conflict of interest.

This article is a PNAS Direct Submission.

Freely available online through the PNAS open access option.

[1]To whom correspondence should be addressed. E-mail: dario@ucla.edu.

This article contains supporting information online at www.pnas.org/lookup/suppl/doi:10.1073/pnas.1118926109/-/DCSupplemental.

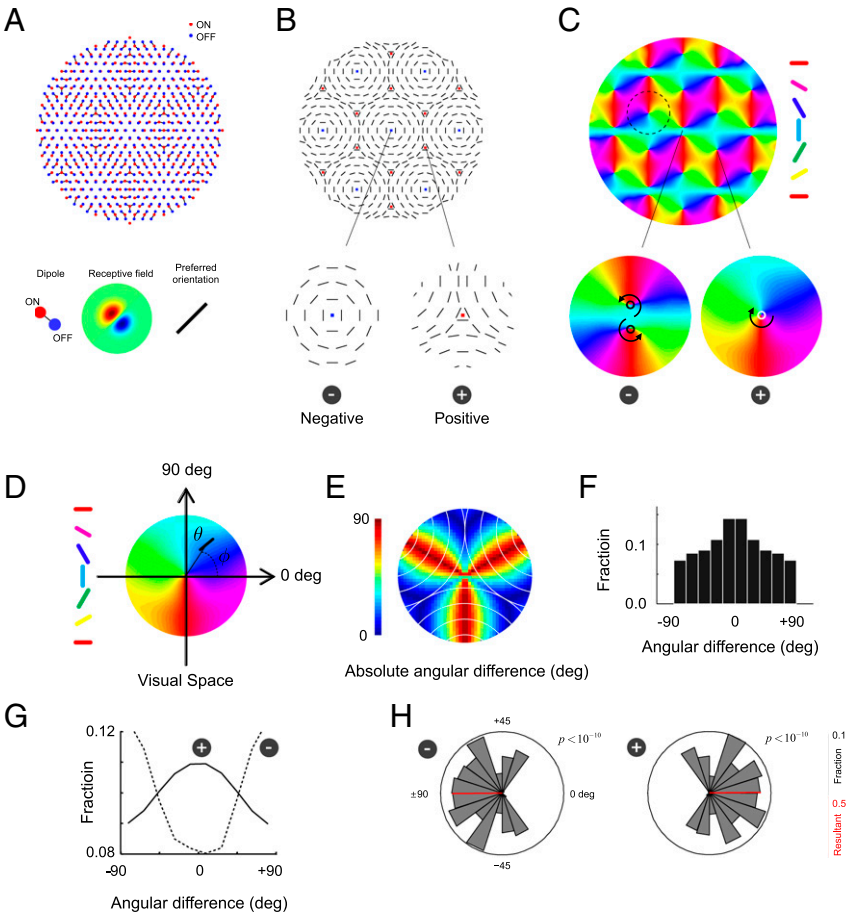

Fig. 1. Moiré interference of retinal mosaics predicts a link between retinotopic and orientation maps. (*A*) (*Upper*) Two hexagonal lattices representing ON- (red) and OFF-center (blue) ganglion cell receptive fields generate an interference pattern that can be described in terms of ON/OFF dipoles. The relative angle between the two mosaics in this example is zero. (*Lower*) A cortical cell with input dominated by a dipole has a receptive field with side-by-side subregions of opposite sign and can be tuned for orientation. The preferred orientation is orthogonal to the line joining the receptive field centers of the ON/OFF that define the dipole. (*B*) (*Upper*) The orientation of dipoles in the interference pattern, indicated by the orientation of short line segments, changes over space, generating a blueprint for an orientation map. The model generates orientation singularities of opposite signs, some with chirality −2 (blue squares) and others with chirality +1 (red squares). (*Lower*) The organization of orientation preferences around negative (*Left*) and positive (*Right*) singularities. (*C*) Pseudocolor representation of the orientation map resulting from the dipole organization in *B* along with the structure of positive and negative singularities. The dashed black circle represents the size of the neighborhood used in subsequent analyses of local angle distributions (the neighborhood radius was 0.3 of the period of the orientation map, which represents 75% of the mean nearest-neighbor distance to the closest singularity). (*D*) Overlaying a retinotopic axis on an orientation singularity allows the assignment of two angles to each point within its neighborhood. One represents the displacement angle with respect to the horizontal meridian (ϕ) and the other represents its preferred orientation angle (θ). A positive singularity is used in this example. (*E*) The local organization of dipole orientation around a positive singularity is dominated by three sets of cocircular arcs (white contours), reflecting the organization in *B*, *Lower Right*. The pseudocolor image shows the absolute value of the angular difference at each location within the neighborhood. Along three directions the difference is large (red areas), but most of the area is dominated by small differences (blue areas). As a result, the distribution of angular differences shows a peak at zero (*F*). (*G*) The same predicted relationship holds when the distributions of the angular differences are calculated using the full model, which samples the RGC mosaics with an isotropic Gaussian function to derive the shape of receptive fields at each location. (*H*) The distribution of mean angles across singularities shows that positive singularities ought to have a resultant near 0°, whereas negative singularities ought to have a resultant at ±90°. Black bar represents the scale for the circular distribution and red bar represents the scale for the resultant vector.

neighborhood of negative singularities, where a cocircular organization of preferred dipole orientations dominates the local organization (Fig. 1*B*, *Lower Left*), the two angles are near orthogonal to each other. Thus, one expects the distribution of the angular differences to peak at ±90°. In contrast, in the neighborhood of positive singularities, the local orientation of the dipoles is dominated by three concentric groups of arcs (Fig. 1 *B*, *Lower Right*, and *E*, white contours). The angular difference in this case changes within the neighborhood. Along three directions joining the center of the negative singularity with those of neighboring positive singularities, the angles are orthogonal to each other (Fig. 1*E*, red regions). However, the area covered by these regions is smaller than those at intermediate locations where the angular difference is small (Fig. 1*E*, blue regions). As a result, the distribution of angular difference over the entire neighborhood shows a broad peak centered at 0° (Fig. 1*F*). These expectations, developed by considering the orientation of ON/OFF dipoles, are confirmed when we calculate the angular difference distributions derived from the actual receptive fields and orientation maps generated by the model (Fig. 1*G*). Thus, the theory predicts positive pinwheels ought to have a distribution of angular differences with a mean near zero, whereas negative pinwheels ought to have a mean near ±90°.

An alternative way to illustrate the prediction is by computing the mean angle of the angular difference distribution independently for each singularity in the map and subsequently forming a histogram of the resulting values for positive and negative pinwheels (Fig. 1*H*). The mean angle for negative singularities is expected to be at ±90° whereas for positive angles it is expected to be zero.

Confirmation of the Predicted Link in Tree Shrew V1. We tested the predicted relationship by analyzing orientation maps from tree shrew primary visual cortex (20). In these maps, the boundary between V1 and V2 is clearly visible and represents the vertical meridian in the visual field (Fig. 2*A*). Moreover, the retinotopic map in tree shrews is near isotropic within the representation of central visual space (21, 22). This relationship allows us to estimate the alignment of the main retinotopic axes (Fig. 2*A*, coordinate system at the center of the orientation map) and to calculate the angular difference distributions at pinwheels of different signs. To avoid boundary effects, we restricted our analyses to regions of interest within the center of the orientation maps (Fig. S2).

Before embarking on the analysis of the experimental data it is necessary to verify that the predictions hold true in a more

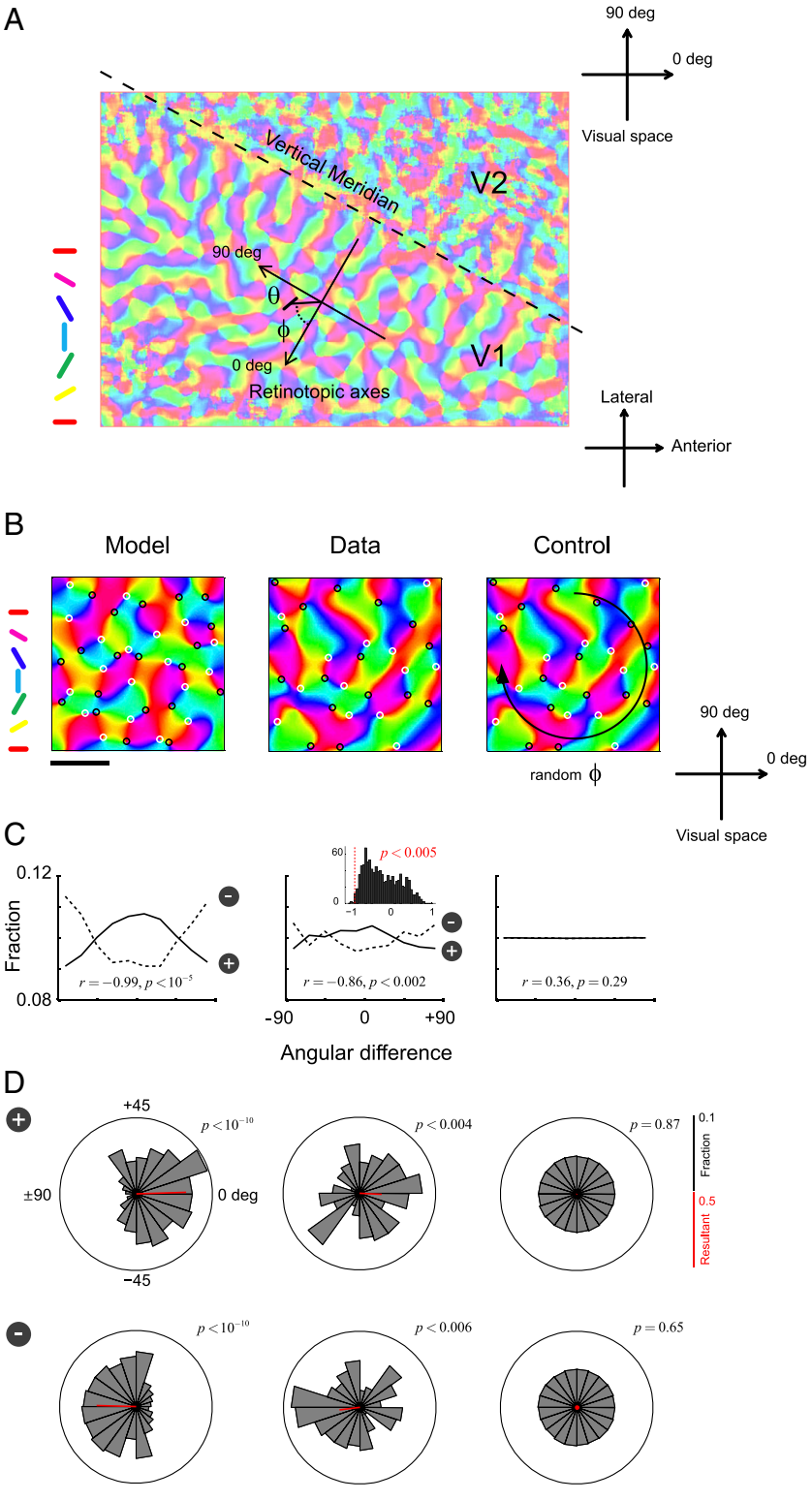

Fig. 2. Predicted link between retinotopic and orientation maps is confirmed in tree shrew primary visual cortex. (*A*) Sample orientation map in tree shrew visual cortex from the work of Mooser et al. (20). The V1/V2 boundary is clearly visible and marked with a dashed line. The orientation of the areal boundary serves to anchor the retinotopic axes within the center of the orientation map where the analyses are conducted. Note that the measurement of the axial angle ϕ must take into account the orientation of the positive axes of the retinotopy. (*B*) Theoretical, experimental, and control orientation maps. In each case we illustrate the orientation map, with detected pinwheels (+1 singularities in white and −1 in black). Note that in the model, which now includes positional noise, only −1 singularities are observed. (*C*) Distribution of average angular differences and their correlation coefficients (calculated by Matlab's corrcoef function). The distribution of correlation coefficients from Monte Carlo simulations by randomly rotating the orientation maps is shown at the *Inset*, with the vertical red line marking the experimental value that achieves a significance level of 0.005. (*D*) Circular distribution and resultant of the mean angle across singularities of different signs (positive on the top and negative on the bottom). The average distributions for the control case are statistically indistinguishable from uniform.

realistic version of the model and over a reasonable range of parameter values. This procedure is required because it became clear during the course of our studies that the location of orientation singularities can shift in the presence of noise (Fig. S3). For example, it turns out the −2 singularities are unstable and readily split into two −1 singularities in the presence of small amounts of RGC noise (Fig. 2*B*, *Left*). Our simulations show that, nevertheless, the predicted link holds and it is robust over a substantial range of noise and scaling factors (Fig. 2 *C*, *Left*, and *D*, *Left* and Fig. S4).

With the assurance that the prediction is robust to changes in parameters and noise levels, we proceeded to test whether the data showed evidence of the predicted link. Remarkably, analysis of the layout of preferred orientations around singularities ($N_p = 170$ positive and $N_n = 178$ negative singularities in five maps) confirms the predicted link between retinotopic and orientation maps (Fig. 2 *B–D*, *Center*). As expected, the average distributions for positive and negative singularities peak at zero and ±90° and are significantly anticorrelated. Moreover, the distribution of the mean angles across singularities of opposite signs differs significantly from uniform and has resultants with the expected angles (Fig. 2*D*, *Center*).

As a control condition, we randomly rotated the five orientation maps with respect the retinotopic axis and repeated the calculations. Each realization of such control condition simulates the outcome of our measurements under the null hypothesis that there is no angular relationship between the retinotopic and orientation maps. In each simulated control experiment, we calculated the correlation coefficient between the distributions for the positive and negative singularities. Using the distribution of the resulting correlation coefficients (n = 1,000 simulations), the probability that the observed value of $r = -0.86$ could have resulted by chance under the null hypothesis is $P < 0.005$ (Fig. 2*C*, *Center Inset*). Thus, the data reject the null hypothesis that retinotopic and orientation maps are independent of each other. Finally, the average distributions in the control condition are, as expected from the randomization procedure, statistically indistinguishable from uniform (Fig. 2 *C*, *Right*, and *D*, *Right*).

To examine in more detail how the angular variables deviate from statistical independence we calculated $\Delta p(\theta,\phi) = p(\theta,\phi) - p(\theta)p(\phi)$ at both types of singularities (Fig. S5). The model predicts that the deviation from independence at positive singularities, $\Delta p^{+}_{\text{model}}$, must show three discrete positive peaks near the unity line and three discrete negative peaks at locations where the angles are offset by ±90° (Fig. 3*A*, *Upper Left*). In contrast, the prediction at negative singularities, $\Delta p^{-}_{\text{model}}$, must show a more diffuse, band-like structure, with negative values aligned with the unity line and positive values aligned at locations where the angles are offset by ±90° (Fig. 3*A*, *Lower Left*).

Remarkably, the measured deviations in the data, $\Delta p^{+}_{\text{data}}$ and $\Delta p^{-}_{\text{data}}$, resemble their theoretical predictions very well (Fig. 3*A*, *Center*). To quantify this agreement and to assess its statistical significance we defined a similarity index by

$$\text{SI}(\Delta p) = \frac{\left\langle \left(\Delta p - \Delta p^{-}_{\text{model}}\right), \left(\Delta p^{+}_{\text{model}} - \Delta p^{-}_{\text{model}}\right) \right\rangle}{\left\| \left(\Delta p^{+}_{\text{model}} - \Delta p^{-}_{\text{model}}\right) \right\|^2},$$

where $\langle \cdot, \cdot \rangle$ is the dot product between the 2D functions. The index is near zero if the argument is close to $\Delta p^{-}_{\text{model}}$ and near +1 if the argument is close to $\Delta p^{+}_{\text{model}}$. We computed the similarity indexes for both the data and controls ($n = 100,000$), each obtained by randomly rotating the five orientation maps in our dataset with respect to the retinotopic axis (one realization of a control is shown in Fig. 3*A*, *Right*). The control data yield a joint distribution of indexes, $\text{SI}(\Delta p^{+}_{\text{control}})$ and $\text{SI}(\Delta p^{-}_{\text{control}})$, under the null hypothesis that the angular variables are statistically independent (Fig. 3*B*, heat map distribution). A perfect agreement between the data and the model would result in similarity indexes for the data falling on the (1, 0) coordinate point on this graph (Fig. 3*B*, red asterisk). The actual indexes are $\text{SI}(\Delta p^{+}_{\text{data}}) = 0.77$ and $\text{SI}(\Delta p^{-}_{\text{data}}) = 0.30$, which places the data closer to the predicted (1, 0) than the cloud of control data points (Fig. 3*B*, white circle vs. heat map). The likelihood that the control set would generate a distribution at positive singularities closer to the model's prediction than the one observed is $P < 0.03$ (Fig. 3*B*, probability of the vertical hatched area); the likelihood that the same would be the case at negative singularities is $P < 0.05$ (Fig. 3*B*, probability of horizontally hatched area); and finally, the likelihood the control would generate data in better agreement with the prediction, simultaneously for both positive and negative singularities, than what is observed is $P < 0.005$ (Fig. 3*B*, probability of cross-hatched area). Thus, the degree of similarity between the data and the model is statistically significant.

Discussion

The present study unveiled a relationship between orientation singularities and the retinotopic map that had, until now, escaped

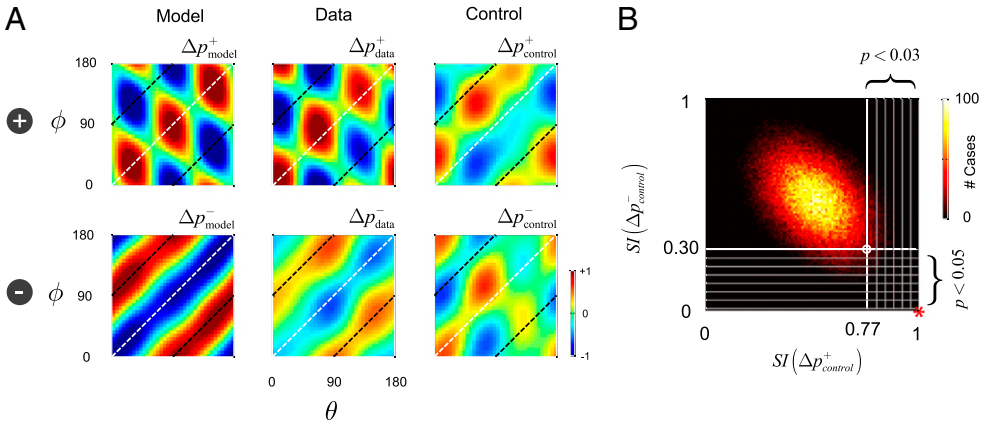

Fig. 3. Deviations from statistical independence. We studied the deviations from statistical independence of the angular variables, $\Delta p(\theta,\phi) = p(\theta,\phi) - p(\theta)p(\phi)$ at positive and negative singularities. (*A*) Model predictions (*Left*), measured deviations (*Center*), and one realization of the control (*Right*). Dashed white lines indicate the unity line $\theta = \phi$, whereas dashed black lines indicate the relationship $\theta = \phi \pm 90°$. (*B*) Joint distribution of $\text{SI}(\Delta p^{+}_{\text{control}})$ and $\text{SI}(\Delta p^{-}_{\text{control}})$ under the null hypothesis that the angular variables are statistically independent. The data have similarity indexes of $\text{SI}(\Delta p^{+}_{\text{data}}) = 0.77$ and $\text{SI}(\Delta p^{-}_{\text{data}}) = 0.30$, as indicated by the white circle. The probability of the vertically hatched area under the null hypothesis is <0.03, that of the horizontally hatched area is <0.05, and that of their intersection is <0.005.

detection. Remarkably, the maps are linked in a way consistent with the prediction of the moiré interference model, explaining the modes of the angular differences (Fig. 2) and the deviation from independence in their joint distributions (Fig. 3).

The theory provides a parsimonious explanation for a diverse set of phenomena. For example, it explains some key features of the statistics of monosynaptic connections between the thalamus and cortex (19). In the model, the sign rule (23), which refers to the tendency for ON/OFF-center inputs to connect to simple-cell subregions of the same sign, is explained by the limited overlap of inputs present in the retinal mosaics (figure 4A in ref. 19). The limited overlap of ON/OFF inputs is also consistent with the clustering of ON- and OFF-center afferents in layer 4 (24) and the finding that the average input from thalamic afferents is biased with a preferred orientation that matches that of the target cortical column (25, 26). The model also explains a tendency for simple-cell receptive fields to have odd-symmetric profiles (27–29), which is a consequence of their inputs being initially dominated by a single dipole that generates an odd-symmetric receptive field (Fig. 1*A* and figure 5 in ref. 16). Moreover, the model provides a simple explanation for the emergence of orientation columns. Namely, a set of neurons within a cortical column that share the same inputs will be biased toward the same preferred orientation. The global structure of the interference pattern accounts for the hexagonal symmetry of orientation maps (16, 18) and a tendency for cocircularity in their organization (30–34). Altogether, the ability of the model to account for these diverse findings lends support to the notion that spatially structured and limited input from the contralateral retina may seed receptive fields and the orientation map during the earliest stages of development (9, 10, 35–51).

One may be surprised that the organization of map structure visualized via optical imaging of signals in layer 2+3, even in species with different laminar architecture (16), would show remnants of a spatially structured retinal input to the cortex. However, we note that the model makes a general statement about the class of linear receptive fields that may be implemented at any one point in the visual field given a limited set of retinal inputs. So long as we restrict ourselves to a linear combination of the retinal signals, the particular anatomical organization of the early visual pathways is immaterial. The class of realizable receptive fields is determined by the structure of the RGC mosaics and the assumption that the input to the first neurons exhibiting orientation selectivity can be well approximated as a linear combination of signals from the retina.

Testing the relationship between the maps discussed here in other species is clearly important. We were limited in our study to the tree shrew because it was the only case that allowed us to estimate the orientation of the retinotopic axes from the orientation of the V1/V2 boundary that was visible in the orientation maps (Fig. 2*A*). Similar tests should be carried out in other species by careful imaging of both orientation and retinotopic maps.

Finally, we note that many important questions emerge in relation to the proposed scheme, which require further research. Are the retinal mosaics sufficiently regular to allow for the proposed spatial interference? What mosaic class is responsible for establishing the orientation map? How precise should the retinotopic map be? How are binocular receptive fields with matching orientation established? Although much remains to be explored, the simplicity and explanatory power of the moiré interference model provide a competing hypothesis that deserves to be seriously explored. More broadly, one may conjecture that spatially structured input from the periphery may also help establish the organization of primary sensory cortices in other modalities (52, 53). It would then be of interest to explore whether the model can be applied to explain the properties of other systems. If these ideas are confirmed, they could transform the way we view cortical maps, their development, and their function.

Methods

Data. The dataset used in our analysis is the one first published in Mooser et al. (20). These orientation maps were generously shared with us by David Fitzpatrick (Max Planck Florida Institute, Jupiter, FL) and his colleagues. A detailed description of the experimental methods by which the maps were obtained can be found in the original study. The dataset consists of five orientation maps that included the boundary between V1/V2 within the imaging window. This dataset allowed us to estimate the alignment of the retinotopic axis (Fig. 2*A*). The region of interest for our analyses was restricted to the central region of the maps to avoid boundary effects (Fig. S2).

Model. The moiré interference model simulated was the same as described previously (16). Briefly, RGC mosaics were simulated by adding various amounts of random displacement to each vertex of a hexagonal lattice that represents the position of ON- and OFF-center receptive fields. The centers of RGC receptive field position vectors are defined by

$$\mathbf{r}_{ij}^{\mathrm{OFF}} = d\mathbf{L}_{ij} + \mathbf{n}_{ij}$$
$$\mathbf{r}_{ij}^{\mathrm{ON}} = (1+\alpha)d\mathbf{R}_{\beta}\mathbf{L}_{ij} + \mathbf{n}_{ij} + \mathbf{n}_0.$$

Here, d represents the grid spacing for the OFF mosaic, $(1+\alpha)d$ represents the grid spacing for the ON mosaic, the matrix

$$R_{\beta} = \begin{bmatrix} \cos\beta & \sin\beta \\ -\sin\beta & \cos\beta \end{bmatrix}$$

represents the relative rotation between the ON and OFF mosaics, $\mathbf{n}_{ij}$ represents 2D, Gaussian (i.i.d.) noise with a SD σ, and $\mathbf{L}_{ij}$ are the vertices of an hexagonal grid,

$$\mathbf{L}_{ij} = \frac{1}{2}\begin{bmatrix} 1 & 1 \\ \sqrt{3} & -\sqrt{3} \end{bmatrix}\begin{bmatrix} i \\ j \end{bmatrix} i,j = 0, \pm 1, \pm 2, \cdots.$$

The SD of the noise, σ, is conveniently expressed as a fraction of the grid spacing, d. The noise-free, ideal model corresponds to $\sigma = 0$. A random relative spatial shift between the two mosaics $\mathbf{n}_0$ can be added. However, except for the particular case where the mosaics have the same period, this shift has no consequence, because a rotation and translation can be written as a rotation around a different center.

The period of the interference pattern on the retina is a multiple, S, of the lattice period, d. We call S the scaling factor, and it is fully determined by the relative orientation and relative period of the component lattices and is given by (16)

$$d_M = \left(\frac{1+\alpha}{\sqrt{\alpha^2 + 2(1-\cos\beta)(1+\alpha)}}\right)d \equiv S \times d.$$

In monkeys we can estimate the scaling factor required to match the average period orientation maps in the cortex to be ~8 (16), which is the nominal value we use here.

The full, statistical wiring model includes a stochastic component that allows cells in the same cortical column to develop slightly different receptive fields (19), as both the probability of connection to an afferent and its synaptic strength are random variables. Here, we did not simulate the whole model but computed only the mean receptive field at each location. We have previously shown the mean receptive field can be computed efficiently as an isotropic Gaussian-weighted sum of the afferent input to the cortical column (8). The profile of the resulting receptive field was analyzed to estimate its preferred orientation and selectivity. Finally, the preferred orientation of well-tuned cells was spatially smoothed to generate the predicted orientation maps. The details of all these procedures are described in ref. 16.

Analysis of Orientation Maps. The analysis of the maps was scaled according to the orientation map period in each case, which we denote by λ (16). As a preprocessing step we minimally smoothed the maps with a Gaussian kernel with $\sigma = 0.05\lambda$. The orientation maps were represented as a complex field, $z = \exp(i2\theta(x,y))$, and singularities were detected by the intersection of the zero crossings of its real and imaginary components following the method described by Kaschube et al. (9).

The neighborhood around each pinwheel used to compute the angular distributions was defined by a disk of radius 0.3λ. This radius was selected to avoid the boundaries of the neighborhood from becoming too close to adjacent pinwheels, as the average nearest-neighbor distance of pinwheels was 0.4λ. Data from all five maps had to be pooled together to obtain

a significant number of pinwheels of both signs to reach a statistically significant result.

A circular *v*-test was used to test for uniformity in Figs. 1*H* and 2*D*, with the alternative being that the mean was zero for positive singularities and ±90° for negative singularities. When circular statistics were used, they were applied to twice the angle to map the orientation domain to the full circle.

Analysis of Joint Angular Distributions. Let us denote by $\Delta^i p^+_{\text{data}}$ the deviation from independence measured for positive singularities in the *i*th orientation map, $i = 1, \ldots, 5$. Similarly, we denote by $\Delta^i p^-_{\text{data}}$ those measured for negative singularities. We combined the data by computing the average shape of the departures from statistical independence by $\Delta p^{+/-}_{\text{data}} = (1/5)\sum_{i=1,\ldots,5} \Delta^i p^{+/-}_{\text{data}} / \| \Delta^i p^{+/-}_{\text{data}} \|$. Each individual realization of the control condition, obtained by randomly rotating the orientation maps, resulted in deviations $\Delta^i p^+_{\text{control}}$ that that were combined in exactly the same fashion.

Theoretical predictions were generated by the same procedure, averaging the deviation from independence, $\Delta^i p^{+/-}_{\text{model}}$, of maps generated by the model. Here we simulated cases with a fixed scale factor of $S = 8$, relative rotation angles ranging from $-4°$ to $+4°$ in steps of 2° (yielding a total of five maps), and positional noise levels matching those of experimental mosaics (16). The simulated maps were large, providing a total of 455 positive and 459 negative singularities that contributed to the prediction. The restriction to rotation angles between $-4°$ and $+4°$ is a consequence of the model, which predicts that only small, relative angular rotations generate scaling factors that can match the period of the orientation maps in the cortex given the typical ratios of ON/OFF-center cell densities in retinal mosaics (figure 1C in ref. 16). Finally, the resulting 2D distributions were, in all cases, filtered with a Gaussian kernel having a SD of 25°.

ACKNOWLEDGMENTS. We thank D. Fitzpatrick (Max Planck Florida Institute), L. White (Duke University), W. Bosking (University of Texas at Austin), and Y. Li (University of California, Berkeley) for sharing existing tree shrew maps with us. We also thank R. Shapley, M. Hawken, D. Fitzpatrick, and J.-M. Alonso for valuable discussion and comments. This work was supported by research Grant EY018322 (to D.L.R.).

1. Mountcastle VB (1957) Modality and topographic properties of single neurons of cat's somatic sensory cortex. *J Neurophysiol* 20:408–434.
2. Hubel DH, Wiesel TN (1959) Receptive fields of single neurones in the cats striate cortex. *J Physiol Lond* 148:574–591.
3. Hubel DH, Wiesel TN (1974) Uniformity of monkey striate cortex: A parallel relationship between field size, scatter, and magnification factor. *J Comp Neurol* 158: 295–305.
4. Tootell RB, Silverman MS, Switkes E, De Valois RL (1982) Deoxyglucose analysis of retinotopic organization in primate striate cortex. *Science* 218:902–904.
5. Grinvald A, Lieke E, Frostig RD, Gilbert CD, Wiesel TN (1986) Functional architecture of cortex revealed by optical imaging of intrinsic signals. *Nature* 324:361–364.
6. Blasdel GG, Salama G (1986) Voltage-sensitive dyes reveal a modular organization in monkey striate cortex. *Nature* 321:579–585.
7. Bonhoeffer T, Grinvald A (1991) Iso-orientation domains in cat visual cortex are arranged in pinwheel-like patterns. *Nature* 353:429–431.
8. Ringach DL (2007) On the origin of the functional architecture of the cortex. *PLoS ONE*, 10.1371/journal.pone.0000251.
9. Kaschube M, et al. (2010) Universality in the evolution of orientation columns in the visual cortex. *Science* 330:1113–1116.
10. Miller KD, Erwin E, Kayser A (1999) Is the development of orientation selectivity instructed by activity? *J Neurobiol* 41:44–57.
11. Swindale NV (1996) The development of topography in the visual cortex: A review of models. *Network* 7:161–247.
12. Goodhill GJ (1997) Stimulating issues in cortical map development. *Trends Neurosci* 20:375–376.
13. Purves D, Riddle DR, LaMantia AS (1992) Iterated patterns of brain circuitry (or how the cortex gets its spots). *Trends Neurosci* 15:362–368.
14. Soodak RE (1987) The retinal ganglion cell mosaic defines orientation columns in striate cortex. *Proc Natl Acad Sci USA* 84:3936–3940.
15. Wässle H, Boycott BB, Illing RB (1981) Morphology and mosaic of on- and off-beta cells in the cat retina and some functional considerations. *Proc R Soc Lond B Biol Sci* 212:177–195.
16. Paik SB, Ringach DL (2011) Retinal origin of orientation maps in visual cortex. *Nat Neurosci* 14:919–925.
17. Chapman B, Stryker MP, Bonhoeffer T (1996) Development of orientation preference maps in ferret primary visual cortex. *J Neurosci* 16:6443–6453.
18. Muir DR, et al. (2011) Embedding of cortical representations by the superficial patch system. *Cereb Cortex* 21:2244–2260.
19. Ringach DL (2004) Haphazard wiring of simple receptive fields and orientation columns in visual cortex. *J Neurophysiol* 92:468–476.
20. Mooser F, Bosking WH, Fitzpatrick D (2004) A morphological basis for orientation tuning in primary visual cortex. *Nat Neurosci* 7:872–879.
21. Bosking WH, Kretz R, Pucak ML, Fitzpatrick D (2000) Functional specificity of callosal connections in tree shrew striate cortex. *J Neurosci* 20:2346–2359.
22. Bosking WH, Crowley JC, Fitzpatrick D (2002) Spatial coding of position and orientation in primary visual cortex. *Nat Neurosci* 5:874–882.
23. Alonso JM, Usrey WM, Reid RC (2001) Rules of connectivity between geniculate cells and simple cells in cat primary visual cortex. *J Neurosci* 21:4002–4015.
24. Jin JZ, et al. (2008) On and off domains of geniculate afferents in cat primary visual cortex. *Nat Neurosci* 11:88–94.
25. Jin J, Wang Y, Swadlow HA, Alonso JM (2011) Population receptive fields of ON and OFF thalamic inputs to an orientation column in visual cortex. *Nat Neurosci* 14: 232–238.
26. Ringach DL (2011) You get what you get and you don't get upset. *Nat Neurosci* 14: 123–124.
27. Movshon JA, Thompson ID, Tolhurst DJ (1978) Spatial summation in receptive-fields of simple cells in cats striate cortex. *J Physiol Lond* 283:53–77.
28. Ringach DL (2002) Spatial structure and symmetry of simple-cell receptive fields in macaque primary visual cortex. *J Neurophysiol* 88:455–463.
29. Sharpee TO, Victor JD (2009) Contextual modulation of V1 receptive fields depends on their spatial symmetry. *J Comput Neurosci* 26:203–218.
30. Lee HY, Kardar M (2006) Patterns and symmetries in the visual cortex and in natural images. *J Stat Phys* 125:1247–1270.
31. Lee HY, Yahyanejad M, Kardar M (2003) Symmetry considerations and development of pinwheels in visual maps. *Proc Natl Acad Sci USA* 100:16036–16040.
32. Hunt JJ, et al. (2009) Natural scene statistics and the structure of orientation maps in the visual cortex. *Neuroimage* 47:157–172.
33. Sigman M, Cecchi GA, Gilbert CD, Magnasco MO (2001) On a common circle: Natural scenes and Gestalt rules. *Proc Natl Acad Sci USA* 98:1935–1940.
34. Braitenberg V, Braitenberg C (1979) Geometry of orientation columns in the visual cortex. *Biol Cybern* 33:179–186.
35. Wolf F (2005) Symmetry, multistability, and long-range interactions in brain development. *Phys Rev Lett*, 10.1103/PhysRevLett.95.208701.
36. Thomas PJ, Cowan JD (2004) Symmetry induced coupling of cortical feature maps. *Phys Rev Lett* 92:188101.
37. Swindale NV, Bauer HU (1998) Application of Kohonen's self-organizing feature map algorithm to cortical maps of orientation and direction preference. *Proc R Soc Lond B Biol Sci* 265:827–838.
38. Erwin E, Miller KD (1998) Correlation-based development of ocularly matched orientation and ocular dominance maps: Determination of required input activities. *J Neurosci* 18:9870–9895.
39. Erwin E, Obermayer K, Schulten K (1995) Models of orientation and ocular dominance columns in the visual cortex: A critical comparison. *Neural Comput* 7:425–468.
40. Miller KD (1994) Models of activity-dependent neural development. *Prog Brain Res* 102:303–318.
41. Swindale NV, Shoham D, Grinvald A, Bonhoeffer T, Hübener M (2000) Visual cortex maps are optimized for uniform coverage. *Nat Neurosci* 3:822–826.
42. Swindale NV (2000) How many maps are there in visual cortex? *Cereb Cortex* 10: 633–643.
43. Swindale NV (1998) Cortical organization: Modules, polymaps and mosaics. *Curr Biol* 8:R270–R273.
44. Niebur E, Worgotter F (1994) Design principles of columnar organization in visual-cortex. *Neural Comput* 6:602–614.
45. Farley BJ, Yu H, Jin DZ, Sur M (2007) Alteration of visual input results in a coordinated reorganization of multiple visual cortex maps. *J Neurosci* 27:10299–10310.
46. Carreira-Perpiñán MA, Lister RJ, Goodhill GJ (2005) A computational model for the development of multiple maps in primary visual cortex. *Cereb Cortex* 15:1222–1233.
47. Goodhill GJ, Cimponeriu A (2000) Analysis of the elastic net model applied to the formation of ocular dominance and orientation columns. *Network* 11:153–168.
48. Chklovskii DB, Koulakov AA (2004) Maps in the brain: What can we learn from them? *Annu Rev Neurosci* 27:369–392.
49. Mitchison GJ, Swindale NV (1999) Can Hebbian volume learning explain discontinuities in cortical maps? *Neural Comput* 11:1519–1526.
50. Kohonen T, Hari R (1999) Where the abstract feature maps of the brain might come from. *Trends Neurosci* 22:135–139.
51. Saarinen J, Kohonen T (1985) Self-organized formation of colour maps in a model cortex. *Perception* 14:711–719.
52. van der Loos H (1976) Neuronal circuitry and its development. *Prog Brain Res* 45: 259–278.
53. van der Loos H, Dörfl J (1978) Does the skin tell the somatosensory cortex how to construct a map of the periphery? *Neurosci Lett* 7:23–30.